Magnetism, symmetry and spin transport in van der Waals layered systems

Hidekazu Kurebayashi[1,*], Jose H. Garcia[2,], Safe Khan[1], Jairo Sinova[3,4], and Stephan Roche[2,5]**

[1]London Centre for Nanotechnology, UCL, 17-19 Gordon Street, London, United Kingdom
[2]Catalan Institute of Nanoscience and Nanotechnology (ICN2), CSIC and BIST, Campus UAB, Bellaterra, 08193 Barcelona, Spain
[3]Institut für Physik, Johannes Gutenberg Universität Mainz, D-55099 Mainz, Germany
[4]Institute of Physics Academy of Sciences of the Czech Republic, Cukrovarnickaa 10, 16200 Praha 6, Czech Republic
[5]ICREA–Institució Catalana de Recerca i Estudis Avançats, 08010 Barcelona, Spain
[*]e-mail: h.kurebayashi@ucl.ac.uk
[**]e-mail:josehugo.garcia@icn2.cat

ABSTRACT

The discovery of an ever increasing family of atomic layered magnetic materials, together with the already established vast catalogue of strong spin-orbit coupling and topological systems, calls for some guiding principles to tailor and optimize novel spin transport and optical properties at their interfaces. Here we focus on the latest developments in both fields that have brought them closer together and make them ripe for future fruitful synergy. After outlining fundamentals on van der Waals magnetism and spin-orbit coupling effects, we discuss how their coexistence, manipulation and competition could ultimately establish new ways to engineer robust spin textures and drive the generation and dynamics of spin current and magnetization switching in 2D materials-based van der Waals heterostructures. Grounding our analysis on existing experimental results and theoretical considerations, we draw a prospective analysis about how intertwined magnetism and spin-orbit torque phenomena combine at interfaces with well-defined symmetries, and how this dictates the nature and figures-of-merit of spin-orbit torque and angular momentum transfer. This will serve as a guiding role in designing future non-volatile memory devices that utilize the unique properties of 2D materials with the spin degree of freedom.

Key points:

- Fabrication of 2D vdW magnetic systems offers unprecedented opportunities for controlling magnetism and spin transport phenomena down to the monolayer limit.
- Many vdW magnetic systems possess a low-symmetry crystalline structure, providing an array of exotic spin-orbit Hamiltonians, together with added richness arising from interface phenomena driven by layer-to-layer registry.
- Understanding the intertwined contribution of spin-spin interaction and interfacial symmetries is crucial for maximizing the full potential of their SOT efficiency.
- This exciting research field of spin transport at the frontier of layered spin-orbit coupling and magnetism will lead to discoveries of new materials, novel transport effects, topological phenomena and unconventional electron correlation physics.

Introduction

Magnetic moments are informational bits such as those in hard-disc drives and the bits are processed by reversing the moment's direction from one to the other between their equilibrium states[2–4]. Since electronic devices operate either with current- or voltage-regulated inputs, efficient control of magnetic moments by an electric means is important for developing future commercially-viable functional spintronic devices such as spin random access memory[5,6]. The spin-orbit interaction is useful in this context because it microscopically couples the electron motion

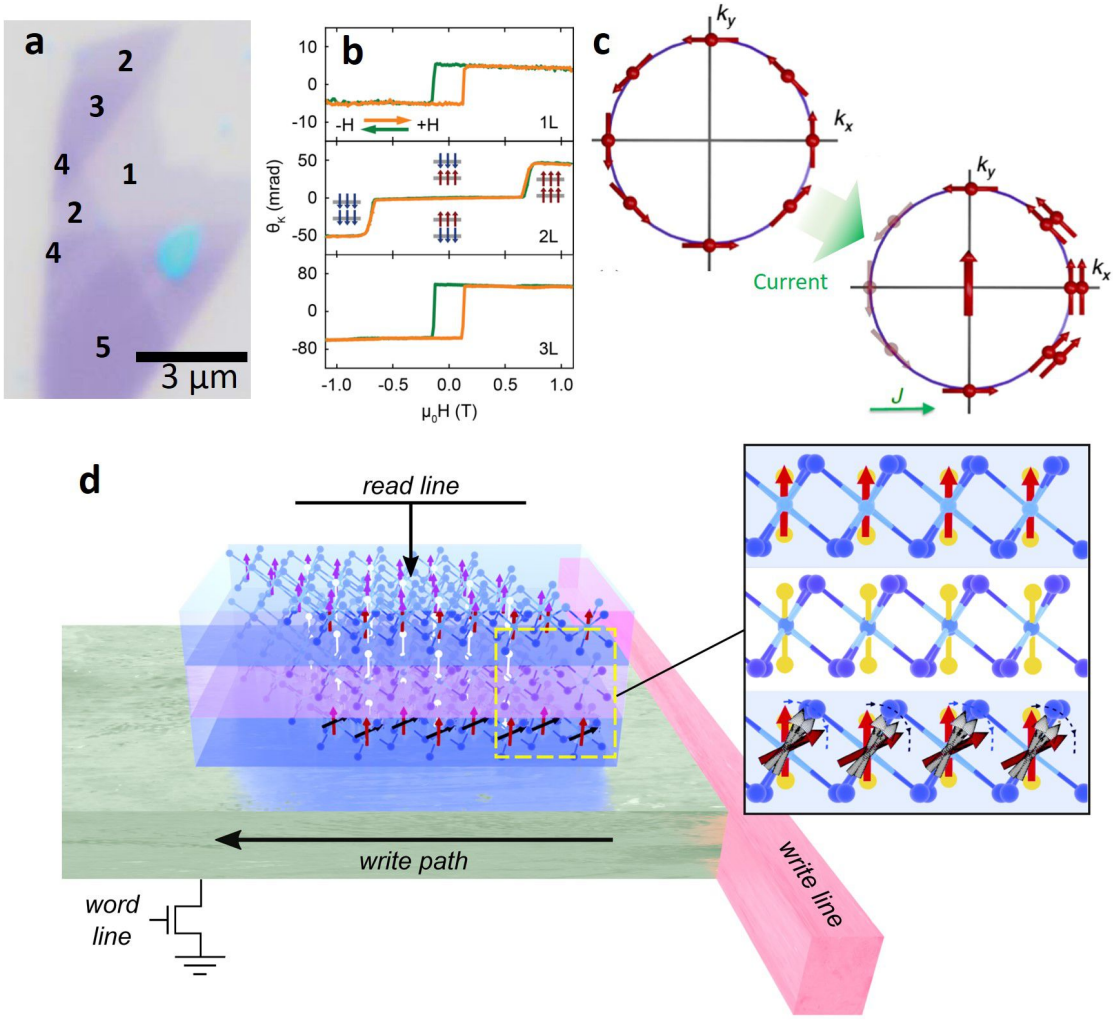

Figure 1. **a** Microscope image of an exfoliated CrI_3 flake. The numbers in the image represent expected monolayer numbers calculated by the image contrast[1]. **b** Magneto-optical Kerr rotation angle measurements applied to the different monolayer number regions while sweeping magnetic field. The monolayer and trilayer regions exhibit a ferromagnetic response, whereas the bilayer region shows an antiferromagnetic behaviour. **c** Rashba spin texture in 2D momentum (reciprocal) space k_x and k_y. For the sake of simplicity, we only show one spin-subband with electrons at each Fermi surface (Left panel). When we apply an electric current along the x direction, electrons are redistributed and as a result, they become spin-polarized due to the spin texture. This is a source of SOT from the Edelstein effect. **d** Schematic of a single-cell of an SOT memory device with vdW magnetic materials. An information bit is stored by the relative orientation of two vdW magnets, which can be read by e.g. magnetoresistance through a vertical current through this stack. An external current is sourced by the write line/path electrode which is a low-resistive material such as copper. This current causes magnetization switching due to SOTs in the bottom vdW magnetic layer as highlighted in the zoom-in figure. The current-supplying bottom electrode could be another vdW material that acts as an additional spin source for boosting the switching efficiency. Figure 1a-b are adapted and modified from Ref.[1].

(current) and the spin degree of freedom, hence making it possible to manipulate spins by electric currents (Fig. 1). Spin-orbit sub-bands in electronic structures (Fig.1c) and/or spin-Hall effect can generate non-equilibrium spin polarisation of conduction electrons that can exert spin torques on local magnetic moments via the exchange interaction. This phenomenon in solid state systems is termed as spin-orbit torque (SOT) which has been discovered and studied mainly in magnetic multilayers with 3D crystals[7–9] and new SOT memory architectures[10] have been proposed and examined in the past several years. Microscopically, SOT originates from two leading effects, the

spin-Hall effect[11] and Edelstein effect[12]. The efficiency and mechanisms of SOT are determined by the electronic states of materials as well as interfaces, in particular inversion symmetry breaking in combination with other crystalline symmetries[13].

2D vdW materials and heterostructures hold great potential to produce unique SOT phenomena as their exotic electronic structures can be modified by interface engineering. The efficiency of magnetization switching by SOT is proportional to magnetic volume[13] and so the smaller the better — the 2D limit is ideal since the volume is minimised along one dimension. In this extreme monolayer regime, it is important to stabilize magnetic orders against thermal fluctuation. This calls for detailed understanding of magnetism at that limit in terms of their driving mechanisms and the strength of them, which can be designed and controlled by material choice and external stimuli. With a full understanding of both magnetism and SOTs in novel vdW heterostructures, we can design highly-efficient spintronic memory cells based on vdW materials (Fig. 1d). In such cells, an information bit is stored by the relative orientation of two vdW magnetic layers separated by another vdW non-magnetic system in the middle. Tunnelling magneto-resistance effect can be used to measure a voltage difference as a read-out. Writing actions for this cell is carried out by a horizontal current which will produce SOT effects to exert magnetic switching of the bottom layer. The efficiency of switching, in terms of electric power, is a key figure of merit since the size of a transistor to drive a current for each cell is determined by this efficiency (a large current implies bigger transistor size) and the cell density is currently limited by the transistor size. This directly means that maximising the SOT efficiency leads not only to low-power consumption of memory cells but also to the high density of data processing. It is important to note that non-magnetic high-spin-orbit vdW materials, such as WTe_2, could be inserted as an additional spin source for SOT-driven magnetization switching. In this regard, a whole variety of vdW heterostructures should be extensively studied for the development of novel vdW spin memory devices.

Over the past five years, magnetic orders have been discovered in several vdW material systems[1,14–18]. Weak mechanical bonding of vdW gaps in these materials offers unprecedented control of individual layer separations by exfoliation, from which we are able to create truly monolayer magnets[1,14] (Fig. 1a,b) and combine them into heterostructures. Unlike other thin-film growth techniques such as molecular beam epitaxy and sputtering, exfoliation of vdW materials allows to stack different vdW monolayers without any thermodynamic constraints, enabling to access an unlimited number of stack combinations to explore fascinating, novel electronic structures[19–21]. This will provide tremendously exciting opportunities to generate new magnetism, spin-transport and electron-correlation physics by using 2D building blocks and currently intensive and extensive research activities on vdW magnetic systems are taking place worldwide. This class of new layered vdW materials is particularly vast, and includes transition metal dichalcogenides[22,23] (TMDs), such as $CrSe_2$, VSe_2, $CrTe_2$, transition metal trihalides[24–26] (CrI_3, $CrCl_3$) and transition metal phosphorous trichalcogenides[27] ($NiPS_3$, $MnPS_3$, etc.). 2D magnetism has been measured at low temperatures in $Cr_2Si_2Te_6$[28], CrI_3[1] and $Cr_2Ge_2Te_6$[14] mono- and bilayers, or in VSe_2[29], Fe_3GeTe_2[16,30] and up to room temperature (RT) in single layer $MnSe_2$[31,32]. In all those materials, the existence of stable magnetic properties for few layered systems is believed to be strongly related to their own magnetic anisotropies as well as the interaction with the substrate that prevents charge density wave instabilities[33–37]. For further discussions on 2D vdW magnetic systems we direct readers to Refs.[38–44], which extensively cover the recent development of 2D vdW magnetic systems and Refs.[45–48] which cover spintronics with non-magnetic vDW materials.

This Review focuses on two fundamental aspects of 2D vdW properties for future spintronic applications. The first is on the exchange interaction as a source of magnetic order by which 2D vdW magnetic systems display different exchange interaction mechanisms depending on their crystalline structures and transport properties from insulators to metals. Understanding of these underlying mechanisms is useful to visualize different magnetic orders at play in a variety of materials and provides a good guide for designing monolayer magnets that are magnetically stable above room temperature (RT). After this, we discuss recent development on electric and other control of equilibrium magnetic states, which is the current state-of-the-art in the relevant field. Second, we discuss SOC effects arising within 2D vdW magnetic materials, through considering their symmetries. Their low-symmetry point groups exhibit a colorful picture of SOT effects and by applying high-throughput point group analysis, we generate and summarize the expected symmetry of SOTs in all the class currently available in the literature. This will aid future SOT experiments using listed materials as well as those newly discovered but possessing the same crystalline symmetry as listed. We further catergorize field-like and damping-like torques existing in these materials as well as more exotic anisotropy-like torques arising from their low-symmetry properties.

Exchange interactions

The magnetic order driven by the exchange interaction of electron spins has different mechanisms, depending on the conductivity regime of materials. This is very relevant to vdW magnetic systems since their conductivity

spans across a wide range, from insulating to metallic regimes (Fig.6a). This is one of the unique potentials of vdW magnetic systems as research topics for current or future materials science for nanomagnetism and spintronic applications. In principle, there is an unlimited number of heterostructure combinations that can be created (conducting/insulating/ferromagnetic) based on the source materials, to explore interface driven phenomena without the constraint of thermodynamics.

The origin of long-range magnetic orders in condensed matter arises from the microscopic exchange interaction between individual spins. The exchange interaction between an array of n spins is usually captured by $H_{\text{ex}} = -\sum_{i,j}^{n} J_{ij}\mathbf{S}_i \cdot \mathbf{S}_j$ where the dot product of $\mathbf{S}_i$ and $\mathbf{S}_j$ represents the relative orientation between the two spins. This Hamiltonian describes how much the spin system gains or loses their total energy by ordering their spin orientations as a whole.

Super-exchange coupling

The exchange interaction model is better suited to describe spins that are well-isolated, such as in the case of magnetic insulators and low-conducting semiconductors, where isolated spins interact with each other via non-magnetic ions (ligands) such as oxygen in their crystal lattices. Such indirect exchange coupling is often called the super-exchange mechanism[49] (Fig.6b). This mechanism can be explained by the virtual excitation of electrons in a magnetic cation and subsequent transmission to the neighbouring cation through the non-magnetic ligand within a timescale of Heisenberg uncertainty. This virtual process effectively lowers the total energy of the system when a long-range magnetic order is present. Magnetic ions for the super-exchange interaction possess the same ionic charge states.

Many vdW materials exhibit semiconducting or insulating properties and this extends to those materials possessing long-range magnetic ordering. CrX_3 (X= I, Br and Cl) exhibits good insulating properties with a typical bandgap energy of 1.2-3.1 eV[1,25,26,50]. In a single layer of CrX_3, each Cr atom is surrounded by X atoms in an octahedral configuration and the Cr atoms form a honeycomb lattice. This crystal field splits the Cr d states into e_g and t_{2g} manifolds where three electrons in their Cr^{3+} state occupy the fully-polarized t_{2g} states with $S = 3/2$ in the valence bands, following the first Hund's rule. These Cr^{3+} moments are coupled through the super-exchange mechanism via an X atom with an approximately 90 degree bonding angle[51,52]. It is noted that due to the presence of finite antiferromagnetic coupling between Cr-Cr direct exchange mechanisms in these materials, the total exchange coupling strength (hence the size of T_C) is relatively weak[53]. A comprehensive study for T_C of few layers of CrX_3 has been carried.[54]. $Cr_2X_2Te_6$ (X=Ge,Si) exhibits semiconductor/insulator properties due to their electronic bands with about a 0.4 eV gap[14,28]. Very much like the case of CrX_3, a honeycomb Cr^{3+} network stabilizes its ferromagnetic order owing to the super-exchange interaction via Te atoms. Another key group of magnetic vdW insulators is those of $MXPS_3$ (M = V, Mn, Fe, Co, Ni, or Zn)[27], with a bandgap of 1.3 - 3.5 eV[55–57]. Transition metals X host magnetic moments within the honeycomb lattice, showing either antiferromagnetic or ferromagnetic order.

Double-exchange coupling

Double exchange coupling takes place in semiconductors. When magnetic ions in a lattice have two types of ionic states, such as Mn^{3+} and Mn^{4+}, an exchange of the two ionic states depends on the spin state of two magnetic ions. This exchange is generated by one mobile carrier (either electron or hole) hopping between the two ions. This hopping is possible when spin states of the two magnetic ions are parallel, leading to delocalisation of the mobile carriers and reduction of their total kinetic energy. This is the double-exchange mechanism[58] that stabilises a long-range magnetic order. A prototypical example of this is $(La_{1-x}Ca_x)(Mn^{3+}_{1-x}Mn^{4+}_{x})O_3$[59]. In this material series, only one type of Mn ionic states exists for both ends of their compositions ($x = 0, 1$), which are good insulators, and the super-exchange interaction stabilises antiferromagnetism in these limits. In their intermediate states, Mn^{3+} and Mn^{4+} coexist (effectively Mn^{4+} being considered as Mn^{3+} and one hole) and a ferromagnetic order outperforms the previously favored antiferromagnetic one via the double-exchange mechanism. In this regime, the presence of mobile carriers is confirmed by the conductivity which becomes several orders greater than those of the insulating compositions.

The double-exchange mechanism has not been discussed extensively in 2D vdW magnetic systems so far, although this mechanism should be commonly present for magnets with moderate electric conduction. As discussed later, $Cr_2Ge_2Te_6$ with chemical and electric doping[60,61] is one example where the exchange coupling strength is modified by the double-exchange mechanism, exhibiting large enhancements of the Curie temperature (T_C) compared to undoped $Cr_2Ge_2Te_6$.

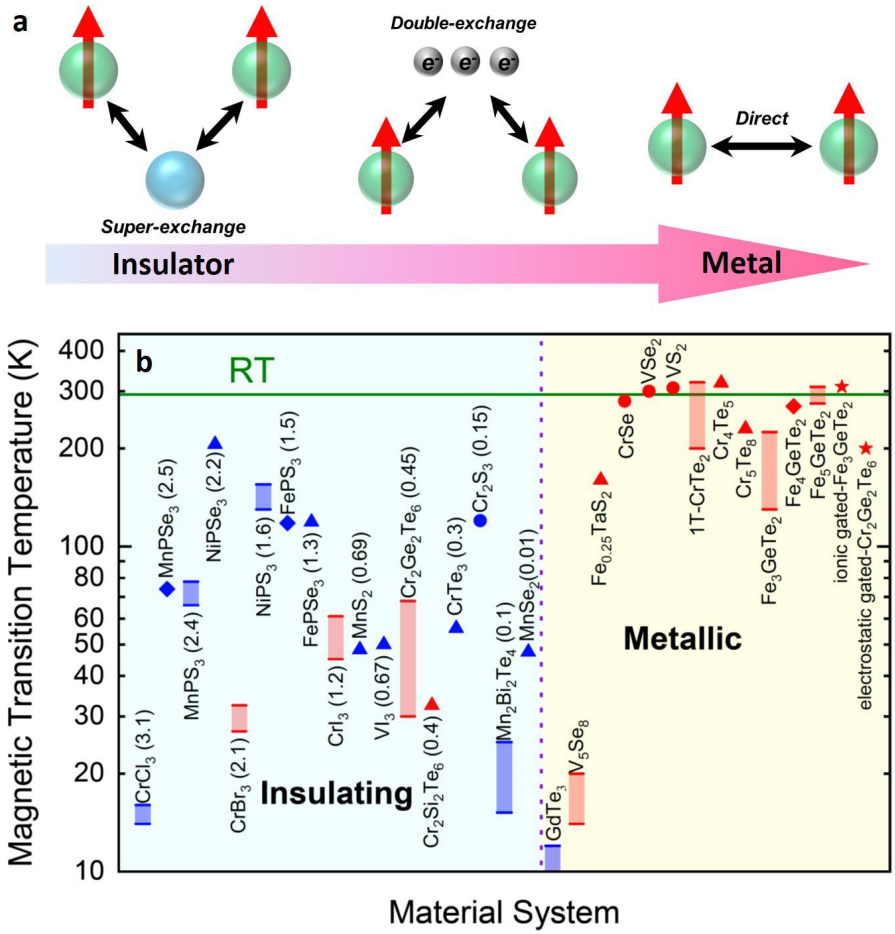

Figure 2. Experimentally validated critical magnetic transition temperature fingerprints for various 2D vdWs magnetic systems. **a** Three different exchange coupling mechanisms of two individual moments as an underlying origin of the long-range magnetic ordering for material systems in the insulating and metallic phases going from left to right. **b** Two-dimensional vdW magnetic materials library showing experimentally determined magnetic transition temperature for materials in insulating and metallic phases. In the insulating phase, number in brackets corresponds to the bandgap value. The dataset is characterised in two-ways using the colours and symbols. Colours: Red (ferromagnetic ordering) and Blue (anti-ferromagnetic ordering). Symbols: Bar (top and bottom points in the bar highlight the transition temperature for bulk and mono/few-layers, respectively), △ (T_C is reported for the bulk case), ◯ (T_C is identified for mono/few-layers), ◊ (T_C is independent of material thickness), and ★ (T_C is enhanced by the external techniques). The data points in the plot are taken from Refs.[1,14,26,29–31,55–57,61–93]

Band magnetism in metals

When conduction electrons are fully delocalized and well hybridized with magnetic ions, we enter the itinerant regime where band magnetism is used to describe the magnetic order. In this mechanism, the total energy of the whole system with respect to magnetic order is described by the energy gain/loss of electrons close to the Fermi energy with the Pauli paramagnetism picture[94]. Based on Pauli paramagnetism, together with the mean-field model[95], the Stoner criterion $D(E_F)U \geq 1$ (where $D(E_F)$ is the density of states (DOS) at the Fermi level in a non-spin-polarized state and and U is the electron correlation energy) can be applied[96,97]. When the Coulomb energy associated with the electron exchange is strong enough, spontaneous exchange-energy splitting takes place to drive ferromagnetism. This model is often employed to discuss the emergence of a magnetic order in metallic ferromagnets[94].

Magnetic vdW materials with electron conductivity are also available, such as VX_2 (X=Se,Te)[29], $MnSe_2$[31], V_5Se_8[85],

Fe-Ge-Te compounds[16,30,92,98], $Fe_{0.25}TaS_2$[86] and Cr-X (X=Te,Se) compounds[76,99,100]. Metallic 2D vdW materials tend to display higher T_C than insulating ones, due to the direct, stronger exchange interaction between individual moments (Fig. 6a). Some of them already possess an above-RT T_C which is relevant to spintronic device applications, although a much higher T_C than RT is welcomed for stable device operation in any of these applications. The Stoner criterion is indeed discussed for some of these materials, such as for Fe_3GeTe_2 in Ref.[93] was calculated to satisfy the inequality by $D(E_F)U = 1.56 \times 0.71 \geq 1$.

A final remark of this section is on the Mermin-Wagner theorem[101] in which an absence of long range magnetic order in spin-rotational invariant systems is introduced. This could be statistically accurate but in reality it is difficult to achieve this since as soon as we make a real magnet, it automatically possesses any sort of magnetic anisotropies, be it from the spin-orbit interaction, anisotropic exchange interaction or magnetic dipole interaction, all of which opens up a gap for magnon excitations that suppress thermal fluctuations.

External control of magnetism

The transport nature in magnets is strongly associated with the type of leading exchange interaction terms and their strength. The exchange interaction can be modified by the carrier concentration as well as the distance between magnetic ions. Here we summarize two external control of magnetism and magnetic states, electric field and strain, applied to 2D vdW magnetic systems.

Electric field

By fabricating a field-effect-transistor (FET)-type device with a thin-film magnet, it is possible to externally control the magnetism by charge accumulation at the surface since the Fermi level and surface carrier density can be modulated. Therefore, this approach is a promising way of controlling the magnetic properties in situ, which has clear relevance to not only achieving high-T_C materials but also gate-tunable spintronic devices. Electric field control of magnetism and magnetic states has been of interest within the field of spintronics where atomically-thin magnetic metals, dilute magnetic semiconductors and magnetic oxides are fundamental and instrumental materials[104]. 2D vdW magnetic systems can offer added values to this already-developed research domain as summarised below.

A dramatic change of magnetism by electric field, probed by modification of T_C, has been observed in several 2D vdW magnets. One study shows parallel-plate capacitor devices with monolayer or bilayer CrI_3 together with a ring-shaped local ac-excitation metal patterns[102] (schematic and microscopy images in Fig. 7a). Magnetic responses from the CrI_3 were measured by magnetic circular dichroism as ac susceptibility (Fig. 7b). A clear change of T_C by applying electrostatic voltages was observed, together with other sizable changes of the saturation magnetization (M_S) and coercive field (H_C), as summarized in Fig. 7c. Bi-layer CrI_3 also exhibits a linear magneto-electric effect due to their magnetic point group with broken spatial-inversion and time-reversal symmetries[70,105–107] . Together with a relatively weak spin-flip transition in CrI_3, the linear magneto-electric effect can shift the transition field and demonstrate pure electric switch between ferromagnetic and anti-ferromagnetic states[70,107] when the applied magnetic field is set at the point of transition while the gate voltage is swept. Another study demonstrated that tunneling magnetoresistance (TMR) can be electrically modified by up to one order of magnitude in four-layer CrI_3 by using bistable magnetic states with the same net magnetization, yet showing different TMR values[108].

An electrostatic modulation of magnetism has been also demonstrated in $Cr_2Ge_2Te_6$[61,109] By applying the gate voltage to a 3.5 nm $Cr_2Ge_2Te_6$ film via a SiO_2 solid-state dielectric, a carrier density of order of 10^{12} cm^{-2} was achieved for both electron and hole doing regimes, and a moderate change of M_S was observed without any significant change of T_C[109]. Using a similar FET-type device with 20 nm thick $Cr_2Ge_2Te_6$ with an ionic gel as a dielectric[61] (Fig. 7d), a much stronger doping action has been observed, at the level of 10^{14} cm^{-2} and T_C of $Cr_2Ge_2Te_6$ is enhanced from 64 K (bulk)[14] to 200 K. This enhancement is explained by the activation of the double-exchange interaction mechanism by introducing a significant number of electrons. In this regime, about one quarter of Cr^{3+} magnetic ions become Cr^{2+}, where hopping of electrons via the Te atoms contributes to the additional exchange mechanism, enhancing the exchange coefficient as well as T_C. With this charge accumulation at the interface, the width of the region where electrons are doped electrostatically becomes comparable to the vdW gap ($\sim$ 1 nm). Therefore, we can create an artificial 2D electron gas together with magnetism within the 20 nm thick $Cr_2Ge_2Te_6$. Furthermore, the magnetic easy axis of $Cr_2Ge_2Te_6$ is switched from out-of-plane to in-plane by this carrier doping[61].

While CrI_3 and $Cr_2Ge_2Te_6$ are magnetic insulators in their pristine forms, the electric field modulation of magnetism has been also explored in metallic itinerant vdW magnets such as Fe_3GeTe_2[30]. A detailed study of the T_C of Fe_3GeTe_2 was done with different layer numbers (Fig.7f) and applied electric fields onto a trilayer Fe_3GeTe_2 film using solid electrolyte ($LiClO_4$ dissolved in polyethylene oxide matrix). T_C is greatly enhanced from 100 K to

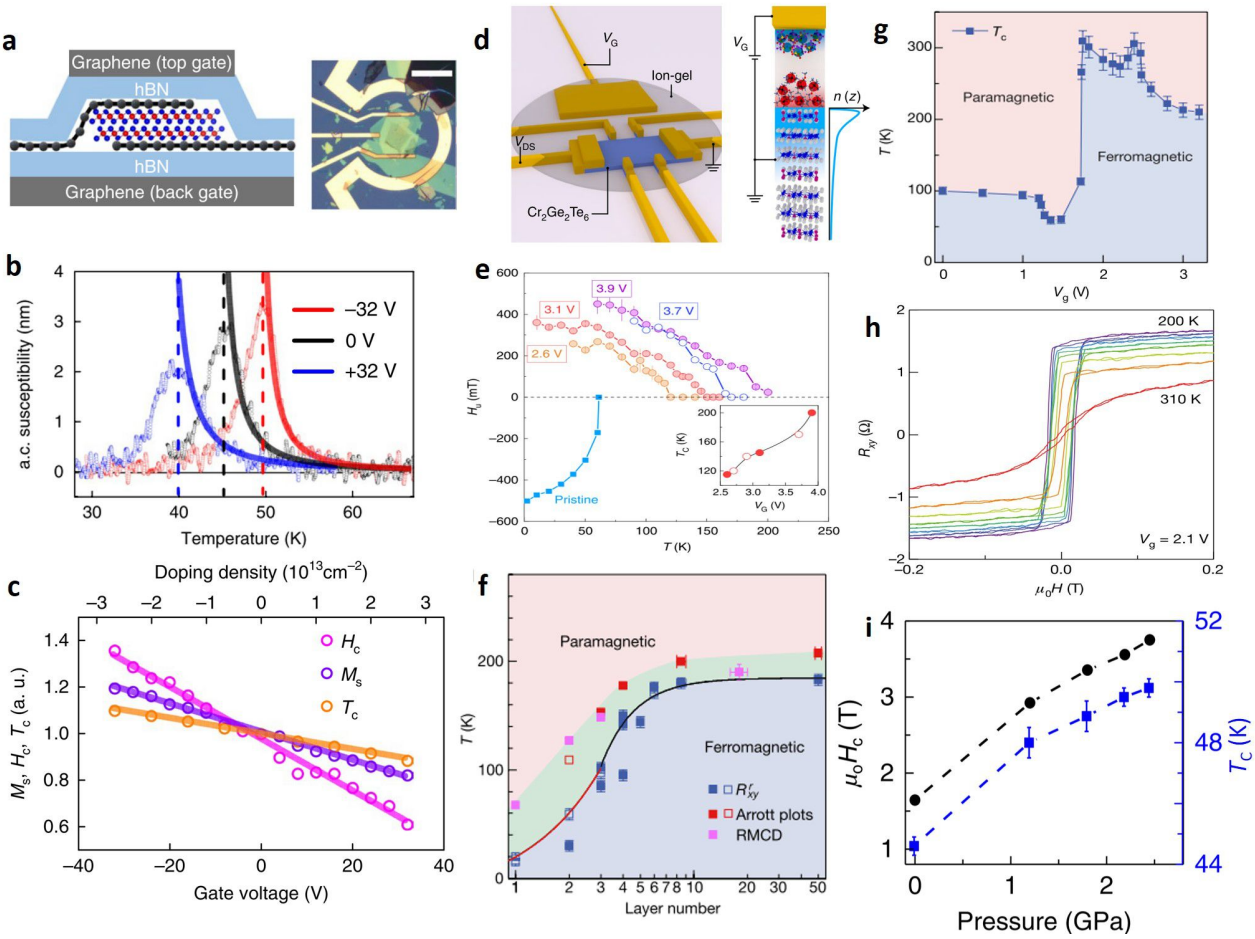

Figure 3. Experimental observation of electric field control of magnetism in different vdW magnets. **a** A schematic side view of a field-effect device with a bilayer CrI_3 encapsulated in few-layer graphene and hBN. The left panel is an optical microscope image for their device with a scale bar of 20 μm. **b** Electric field control of magnetism in measured by ac susceptibility with different gate voltages as shown. **c** Coercive force (magenta), saturation magnetization (purple) (both at 4 K) and Curie temperature (orange) normalized by their values at zero gate voltage as a function of gate voltage and induced doping density. **d** Schematics of a field-effect-transistor device with $Cr_2Ge_2Te_6$ and side view of charge accumulation by electric field. **e** Experimentally-deduced out-of-plane anisotropy field in $Cr_2Ge_2Te_6$ as a function of temperature for different gate voltages, with T_C with gate voltages (inset). **f** T_C of Fe_3GeTe_2 with different layer thicknesses measured by different analysis methods shown. **g** Gate voltage dependence of T_C in a trilayer Fe_3GeTe_2 and **h** their hysteresis loops for different temperatures. **i** the extracted critical field for spin-flip transition (black circles) and critical temperature (blue squares) as a function of pressure in a trilayer CrI_3. Figures are adapted from Ref.[102] (Fig. 3a-c), Ref.[61] (Fig. 3d-e), Ref.[30] (Fig. 3f-h) and Ref.[103] (Fig. 3i) respectively.

above 300 K by application of around 2 V (Fig. 7g&h). This gate-tunability of T_C can be understood by the Stoner model[96,97] since the energy gain by forming a ferromagnetic phase depends on the size of DOS at the Fermi level. Theoretical calculations suggest that by applying the electric field, the Fermi level can be lifted up to a large DOS peak area in Fe_3GeTe_2, mainly consisting of Fe d_{z^2}, d_{xz} and d_{yz} orbitals[30]. The non-monotonic behaviour of T_C as a function of gate voltage may imply this Fermi level passing by the peak points.

Strain

Strain is also a good external knob to modify the magnetic ground state of 2D vdW magnets. In some of these magnetic materials, the interlayer exchange coupling governs the ground-state spin orientation, leading for instance to antiferromagnetism in CrI_3. Since the exchange coupling is very sensitive to the distance between two spins (in

this case, the vdW gap distance), any external perturbation modifying this length enables the control of magnetism, as shown with hydrostatic pressure of few GPa which can induce change of T_C of bulk vdW crystals $Cr_2Ge_2Te_6$[110], CrI_3[111] and VI_3[73] as well as the sign change of the two-fold magnetic anisotropy in $Cr_2Ge_2Te_6$[112]. In the thin-film regime, two studies[103,113] both independently applied hydrostatic pressure of a few GPa on a few monolayer of CrI_3 and observed a monoclinic-to-rhombohedral structural transition, driven by interlayer antiferromagnetic or ferromagnetic couplings[114–117]. Similarly, a ferromagnetic-antiferromagnetic transition under applied pressure, as well as pressure-controlled magnetic state switching between antiferromagnetism to ferromagnetism have been also demonstrated[103]. Such monoclinic-to-rhombohedral structural transition can be also observed in exfoliated $CrCl_3$ crystals with a variation of the interlayer exchange coupling by up to one order of magnitude, when compared to bulk samples[118]. This result highlights that sample fabrication processes unintentionally produce strain that greatly perturbs the magnetic properties of exfoliated magnets. Whether this monoclinic phase is from thermodynamic ground states or meta-stable states induced by their exfoliation processes is yet to be revealed[118]. Furthermore, T_C can be modified by application of strain, for example a trilayer of CrI_3 (Fig. 7i).

Spin-orbit torque in 2D materials

While the magnetic properties have been successfully controlled in a certain number of 2D vdW magnets, the access to out-of-equilibrium regimes in such materials by using electric currents and other means presents formidable challenges, but also holds paramount potential for future spintronic memory and logic applications[6,119–121]. This area of research is growing fast but to date only a very limited number of reports are available in the literature[122–127]. Non-equilibrium spin polarization can result in substantial angular momentum transfer and magnetization control. This has been achieved using non-collinearity between two magnets[128] in magnetic tunnel junctions, or via the intrinsic SOC of materials[13]. In this section, we start with an overview of the latest experimental demonstrations of magnetization control by electric currents with 2D vdW materials, and then present a theoretical analysis of spin torque physics.

Experimental results

TMDs with large spin-orbit coupling (SOC), such as WTe_2 and $NbSe_2$, have already been employed to generate spin torques in ferromagnetic metals[122–124]. For example, the torque symmetry arising in $NiFe/WTe_2$ bi-layers results from the symmetry lowering at the interface[122], exhibiting the damping-like symmetry with the spin-polarization along the out-of-plane direction which cannot be generated by the spin-Hall effect[13]. Magnetic moments in vdW ferromagnets have been also manipulated by current-induced spin torques[125–127]. Interestingly, the spin-Hall effect in Pt was used to generate spin currents into $10 \sim 20$-nm-thick exfoliated Fe_3GeTe_2 thin-films, and induce magnetization switching for low current density of 2.5×10^{11} A/m^2[125,126]. This current density is actually comparable to the one needed to switch standard 3D transition metal alloys[13]. A magnetization switching by the spin-Hall effect has been also discussed in the insulator-$Cr_2Ge_2Te_6$/Ta system, requiring current density of $\sim 5 \times 10^{11}$ A/m^2, comparable to the one necessary for $Tm_3Fe_5O_{12}$[129]. Finally very recently, using current density of about 3.9×10^{12} A/m^2, a spin-orbit torque induced magnetization switching in an all vdW heterostructure was also reported in Fe_3GeTe_2/WTe_2 stacks[130].

So far, the majority of studies on current-induced spin-torque manipulations in 2D vdW magnets exploit the properties of conventional heavy metals to generate the spin source. Due to the intrinsically low crystalline symmetry of vdW materials, some 2D vdW magnets lack an inversion center in their crystalline structures, hence allowing for spin-orbit Hamiltonians with linear or cubic momentum. This fundamentally means that these materials possess spin textures in momentum space which can be tailored by electric currents for magnetisation control[12,13]. While spin-orbit torque arising from spin-textures in momentum space has been demonstrated and studied in great detail in 3D crystals[7,131–133], including the demonstration of damping-like torques due to the Berry-curvature[134], to date no such result have been reported in 2D vdW magnets. Since electronic states in 2D vdW materials are inherently very sensitive to any perturbation caused at interfaces, the 2D vdW material family offers a fascinating and promising playground to explore novel and efficient current-induced spin torques with a large number of possible heterostructure combinations. To guide this research development, we here present a summary of possible spin-orbit torque symmetries for different point group crystals, including the contributions emerging at interfaces. We remind the reader that following Neuman's principle, it is the point group which governs the allowed types of linear response tensors, being themselves translation invariant, and that it is the space group of the material which conditions the band structure, which can have an effect on the magnitude of the response[135].

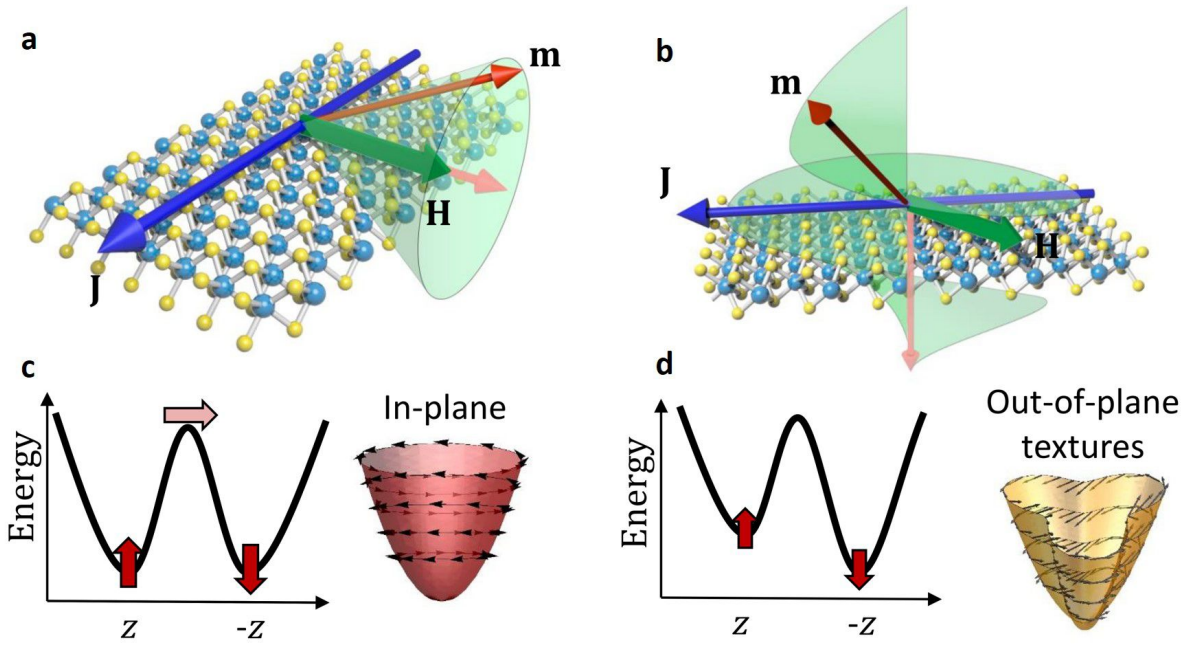

Figure 4. Illustration of spin-orbit torque mechanisms for different spin-textures and their effects on the magnetic energy profile. **a** Magnetization dynamics due to a typical effective SOT field for systems with multiple orthogonal mirror planes. **b** Magnetization dynamics for effective SOC fields with a component parallel to the anisotropy axis. **c** Magnetic energy density for a system with perpendicular magnetic anisotropy and a weak in-plane effective SOC field produced an in-plane spin texture. **d** Magnetic energy density for a system with perpendicular magnetic anisotropy and an effective field with a component parallel to the anisotropy axis, and the spin-textures that enable these kind of fields.

Magnetic torque and spin-orbit interaction

The magnetization in ferromagnetic materials, $\mathbf{M}$, originates from the spin angular momentum $\boldsymbol{s}$ of lattice atoms. The exchange interaction enforces the magnetic order but since it is generally isotropic, a source of magnetic anisotropy is required to dictate the direction of the magnetization at equilibrium, and to stabilize the magnetic phase. Typically, this magnetic anisotropy defines two equilibrium positions along the positive and negative directions along a particular axis, which is characterized by two symmetric minima in the system's energy. An external magnetic field with a component parallel to such an axis will then favor a particular minimum and translates into a torque $\mathbf{T}$ on the magnetization, which will align it along the field direction. Still, large fields are required to induce stable and reversible switching, a condition which remains a significant technological challenge. An alternative way is provided by manipulating the SOC to produce electrically driven torques on the magnetization, known as SOT[136](Fig.8).

SOC is the consequence of the periodic electrical potential due to the nuclei within the crystal, which is felt by the electrons as an effective magnetic field $\mathbf{B}_{\text{soc}}$ proportional to its angular momentum $\mathbf{L}$[137]. The characteristics of the coupling between the spin and this effective field dictate the resulting strength and symmetry properties of the dominant SOC terms. Additionally, the spin of the conduction electrons propagating through a magnetic material will couple to its total magnetization through a Zeeman-like interaction $-(2\Delta_{\text{ex}}/\hbar)\boldsymbol{s}\cdot\mathbf{m}$, where $\hbar$ the reduced Planck's constant[138], $\mathbf{m}\equiv\mathbf{M}/|\mathbf{M}|$ the normalized magnetization, and Δ_{ex} the effective exchange interaction between the localized and itinerant spins. Therefore, in magnetic systems with SOC, the spin of conduction electrons will be driven by the torque produced by a combination of the exchange field $\boldsymbol{B}_{\text{ex}}\equiv-(2\Delta_{\text{ex}}/\hbar)\mathbf{m}$[138,139] and the effective momentum-dependent spin-orbit field $\boldsymbol{B}_{\text{soc}}(\boldsymbol{p})$[137]. Conversely, the action-reaction law states that the magnetization will feel an opposite momentum-dependent torque due to the electronic spin $\mathbf{T}_{\text{soc}}(\boldsymbol{p})$ and will be then indirectly coupled to spins of the itinerant electrons which are also affected by the SOC[140]. We should remember however that since $\mathbf{B}_{\text{soc}}$ is a relativistic effect, it does not exists in the laboratory frame. As a result, any non-zero torque induced by this field will cancel in equilibrium owing to time-reversal symmetry invariance. Nevertheless, under the action

of an external electrical bias ΔV, electrons around the Fermi level E_F are bestowed with extra energy that promotes a reorganization of charge favoring electrons with momentum parallel to the electric field. This non-equilibrium state opens the possibility of a finite non-equilibirum spin density, an effect first discovered by Edelstein[12] and referred to as inverse spin galvanic[13]. This non-equilibrium spin density can also be understood as stemming from an effective macroscopic SOC field $\mathbf{H}_{\text{soc}}(\Delta V)$, that is a function of the bias and promotes a macroscopic torque $\mathbf{T}_{\text{soc}} = \mathbf{M} \times \mathbf{H}_{\text{soc}}$. In this sense, the bias provides the energy to maintain spins alignment with $\mathbf{H}_{\text{soc}}(\Delta V)$, and it will also affect the magnetization direction through the exchange interaction. The direction and strength of this field will actually depend on the average of the momentum-dependent spin polarization, which is usually termed as spin texture and is computed as the expectation value of the spin operators in Bloch's states. In Fig.8c, a sketch of this phenomenon is shown, where the surface represents the allowed energies ($E(\boldsymbol{p},\boldsymbol{s})$) and the arrows indicate the spin texture pattern. In the chosen situation, the spin texture compensate after summation over all allowed momentum. Alternatively, we could also consider the field $\mathbf{H}_{\text{soc}}$ as an electrically induced non-equilibrium magnetic anisotropy that promotes the alignment along a different orientation[141].

In systems with an inversion center, the Bloch states are doubly degenerate for any given momentum, leading to two superimposed and opposite spin textures that will suppress any possible spin torque[142]. This result implies that the SOTs requires a broken inversion symmetry, as typically achieved through the creation of an interface. In layered materials though, the inversion symmetry can be lifted by multilayer stacking[143,144], strain[123], or even the interaction with the substrate[125]. The second class of highly symmetric 2D systems are those possessing a 4-fold rotation axis or higher. At the Γ point of those systems, only in-plane fields perpendicular to the layer and the current such as the one illustrated in Fig.8a are allowed by the in-plane spin textures (Fig.8c) enforced by the symmetries[145]. In systems with perpendicular magnetic anisotropy, such a field will gradually reduce the barrier in Fig.8c without favouring any particular minima, and therefore, cannot produce deterministic switching. However spin-pseudospin coupling[146] and other internal degrees of freedom could lead to nontrinvial out-of-plane textures[147,148], a possibility that remains largely unexplored in the past. In fact, currently the role of symmetries is under extensive experimental study due to its potential for technological applications[122,149]. Exploiting this out-of-plane spin texture (Fig. 8d) is particularly rewarding since it breaks the energy degeneracy of the moment pointing $\pm z$ directions by an electric current as shown in Fig. 8b&d. This leads to deterministic control of the magnetization switching by an electric current without any needs of external magnetic fields in such spintronic switching devices.

Symmetries of spin-orbit torque

The quantitative determination of spin-textures in momentum space requires knowledge of the microscopic interactions at play, which are complicated to measure. Still, they lead to the SOT which is a macroscopic observable, or equivalently, an effective magnetic field $\mathbf{H}_{\text{soc}}$. The underlying lattice, equilibrium magnetic symmetries and atomic structure fully define the SOC and, as consequence, will also determine the allowed SOT symmetries. Moreover, crystal symmetries will also manifests in the torque's dependence on the enforced current $\mathbf{J}$ and the magnetization direction $\mathbf{m}$[139]. In general, $\mathbf{H}_{\text{soc}}$ can be written in terms of the current and magnetization[139,150–152].

To illustrate the method, we will limit ourselves only to terms linear in the current and the magnetization. We already determined that a non-equilibrium state is mandatory to produce the spin-orbit fields forcing it to be proportional to current density at lowest order. Its dependence against the magnetization direction is more complicated since there are two possible contributions,

$$\mathbf{H}^{e} \equiv \Upsilon \mathbf{J}, \tag{1}$$

independent of magnetization and linked to the current density through the 3×3 matrix Υ, and

$$\mathbf{H}^{o} \equiv \mathbf{m} \Lambda \mathbf{J}, \tag{2}$$

which is proportional to the magnetization and is mixed linearly with the current density through the rank-3 tensor Λ. The superscript e/o are included to highlight the even and odd dependence of these fields against magnetization reversal. These two objects comprises over 36 terms that need to be determined to fully describe the torque's symmetries. Through symmetry analysis, these elements can be further reduced to up to two parameters.

To outline how this symmetry analysis work, we will first start by defining a point symmetry $\mathcal{R}$, which is a geometric operation that leaves the positions of the system invariant with respect to a given point, and are representable as 3×3 unitary matrices if we represent positions as 3D vectors. The main assumptions of symmetry analysis is that a representation of these symmetries will also act on all crystal's physical properties, which is

known as Neumann's principle[139,142]. In this sense, both the current density and magnetization must remain invariant against the action of all system's symmetries $\{\mathcal{R}_1, \mathcal{R}_2, \ldots, \mathcal{R}_N\}$, where N is the total number of symmetry operations. This will lead to a set of coupled equations that will restrict the number of allowed components. In general, one must evaluate the N symmetries present in the material, but by using group theory it is possible to reduce it to a much smaller minimal set of symmetries known as the generating set, that can be combined to span the whole group[142], and it is sufficient to impose invariance only in that set.

To wrap up and settle the concepts presented here, we provide an example in Box 1, which illustrates how to use the symmetry analysis to determine the allowed torques of the C_{3v} point group. This group possesses six symmetry elements but a generating set of only two, which we choose to be a rotation of 120° and an reflection on the zy plane, which are generic for 2D honeycomb structures and serve as a starting point to describe many different materials such as graphene heterostructures[153], hexagonal transition metal dichalcogenides, Fe_3GeTe_2[154], CrI_3. Materials belonging to higher symmetry groups such as D_{6h} or C_{6v} will possess fewer allowed torques.

Textbox

The C_{3v} point group of symmetries possess a generating set given by a 120° rotation around the z-axis and a reflection on the yz plane. For any possible symmetries $\mathcal{R}$, the matrices Υ and Λ must satisfy the following set of equations[139,155] $\Upsilon = \det(\mathcal{R})\mathcal{R}\Upsilon\mathcal{R}^T$ and $\Lambda^i = \sum_{i'=x,y,z}\mathcal{R}_{i,i'}\mathcal{R}\Lambda^{i'}\mathcal{R}^T$, where $i,j,k \in (x,y,z)$ defining the direction of the axes of a chosen Cartesian system. Below we show how these tensors change after successive application of the two symmetries.

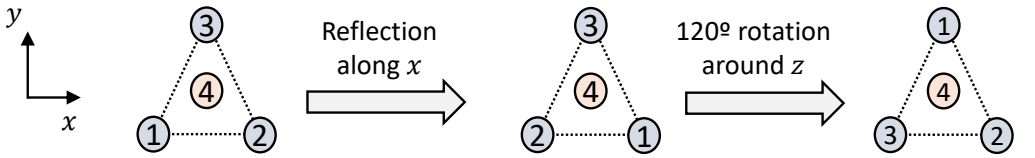

$$\mathbf{H}^e_{\text{soc}} \quad \begin{pmatrix} \Upsilon_{xx} & \Upsilon_{xy} & \Upsilon_{xz} \\ \Upsilon_{yx} & \Upsilon_{yy} & \Upsilon_{yz} \\ \Upsilon_{zx} & \Upsilon_{zy} & \Upsilon_{zz} \end{pmatrix} \quad \begin{pmatrix} 0 & \Upsilon_{xy} & \Upsilon_{xz} \\ \Upsilon_{yx} & 0 & 0 \\ \Upsilon_{zx} & 0 & 0 \end{pmatrix} \quad \begin{pmatrix} 0 & -\Upsilon_{yx} & 0 \\ \Upsilon_{yx} & 0 & 0 \\ 0 & 0 & 0 \end{pmatrix}$$

$$\mathbf{H}^o_{\text{soc}} \quad \begin{pmatrix} \Lambda^x_{xx} & \Lambda^x_{xy} & \Lambda^x_{xz} \\ \Lambda^x_{yx} & \Lambda^x_{yy} & \Lambda^x_{yz} \\ \Lambda^x_{zx} & \Lambda^x_{zy} & \Lambda^x_{zz} \end{pmatrix} \quad \begin{pmatrix} 0 & \Lambda^x_{xy} & \Lambda^x_{xz} \\ \Lambda^x_{yx} & 0 & 0 \\ \Lambda^x_{zx} & 0 & 0 \end{pmatrix} \quad \begin{pmatrix} 0 & -\Lambda^y_{yy} & \Lambda^y_{yz} \\ -\Lambda^y_{yy} & 0 & 0 \\ \Lambda^y_{zy} & 0 & 0 \end{pmatrix}$$

$$\begin{pmatrix} \Lambda^y_{xx} & \Lambda^y_{xy} & \Lambda^y_{xz} \\ \Lambda^y_{yx} & \Lambda^y_{yy} & \Lambda^y_{yz} \\ \Lambda^y_{zx} & \Lambda^y_{zy} & \Lambda^y_{zz} \end{pmatrix} \quad \begin{pmatrix} \Lambda^y_{xx} & 0 & 0 \\ 0 & \Lambda^y_{yy} & \Lambda^y_{yz} \\ 0 & \Lambda^y_{zy} & \Lambda^y_{zz} \end{pmatrix} \quad \begin{pmatrix} -\Lambda^y_{yy} & 0 & 0 \\ 0 & \Lambda^y_{yy} & \Lambda^y_{yz} \\ 0 & \Lambda^y_{zy} & 0 \end{pmatrix}$$

$$\begin{pmatrix} \Lambda^z_{xx} & \Lambda^z_{xy} & \Lambda^z_{xz} \\ \Lambda^z_{yx} & \Lambda^z_{yy} & \Lambda^z_{yz} \\ \Lambda^z_{zx} & \Lambda^z_{zy} & \Lambda^z_{zz} \end{pmatrix} \quad \begin{pmatrix} \Lambda^z_{xx} & 0 & 0 \\ 0 & \Lambda^z_{yy} & \Lambda^z_{yz} \\ 0 & \Lambda^z_{zy} & \Lambda^z_{zz} \end{pmatrix} \quad \begin{pmatrix} \Lambda^z_{yy} & 0 & 0 \\ 0 & \Lambda^z_{yy} & 0 \\ 0 & 0 & \Lambda^z_{zz} \end{pmatrix}$$

The matrix Y is antisymmetric and translate into a cross product between the current and the rotation axis $\mathbf{H}^e = \Upsilon_{yx}\mathbf{J} \times \hat{\mathbf{z}}$. The second term is less straightforward but it is, still, fully defined by just five parameters, that reduces to three for 2D materials. This is a substantial reduction in the number of degree of freedom that one would, e.g., use in a phenomenological fit of the experiment. Also, note that a microscopic calculation would automatically give such reduction, which can be used as a check, or simply one can use the symmetry to reduced calculation cost.

A key feature of 2D materials and their combination is the possible variability of symmetry situations, including interface-induced symmetry breaking[125,153,156–158]. For instance, stacking different 2D materials lifts the inversion symmetry and can artificially enhance the SOC and exchange interaction[143,152,159–162]. Accordingly, it is possible to design and tailor the SOT symmetry by the choice of materials and the engineering of 2D material stacking. There are several studies that show how symmetries affect the magnetization dynamics through a 2D layer inserted at an interface[122,123,127,162–166]. However, 2D magnets can also display an internally generated SOT due to their combined SOC, broken inversion symmetry, and exchange interactions, without needing an interface or spin-injection from an

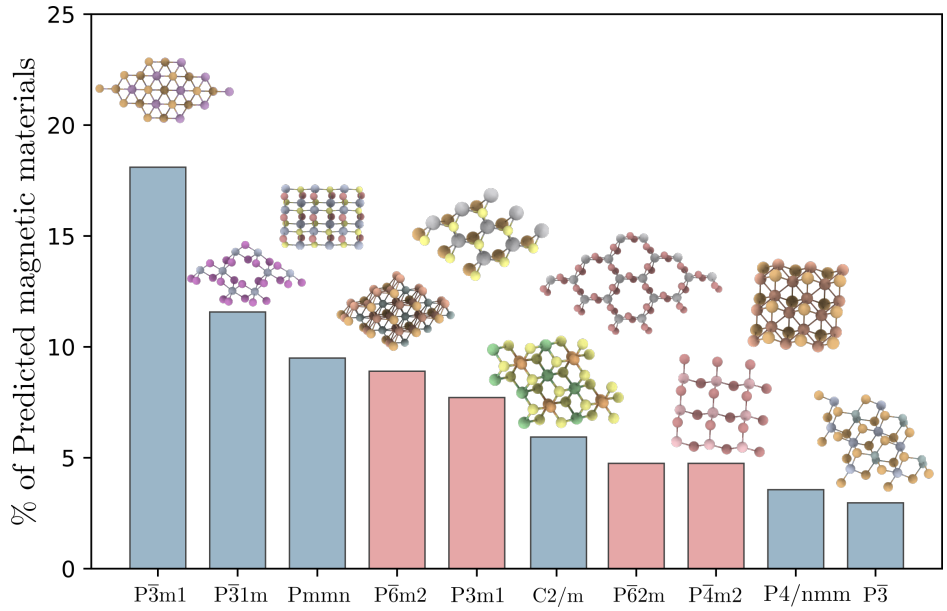

Figure 5. Distributions of magnetic materials predicted using first principle calculations as a function of their Symmetry. The materials family, which requires a substrate-induced inversion symmetry breaking to generate torque components, is identified by the filled blue histograms. Non-centrosymmetric materials which may manifest SOT are outlined by filled red histograms.

adjacent layer, which opens the door for all-in-one SOT-memories. To date, the number of synthesized 2D magnetic materials is still very limited, but novel materials and combinations emerge regularly. Most of the presently known systems belong to the same spatial group and hence will display the same kind of torques.

Material screening and grouping

We here perform a brute-force screening of all possible 2D magnetic materials in the C2DB database[167] and group them according to their symmetry. To do this, we selected only those that were predicted to be stable in their freestanding form according to the database's stability criteria[167]. We also discarded all materials without a point group symmetry since we will restrict the discussion to those materials where symmetry analysis is able to provide physical insights of the torques based on its point group. The final result is presented in Fig. 9, where it is clear that hexagonal and trigonal systems are ubiquitous, in agreement with the trends observed in experimental synthesis. Table 1 provides allowed torques for the most common space groups and gives examples of representative materials that could display them. The space group is shown in the international notation, and we set the z-axis as the high-symmetry rotational axis and aligned the x-axis to one of the lattice vectors. The table is ordered based on the number of symmetry operators in each group, or equivalently, from the highest-to-lowest symmetric groups. In this sense, it is clear that the lowest symmetry group C2/m requires, in general, 12 parameters to define all possible torques, whenever the highest symmetry group is limited to three parameters. The table also reinforces the result presented in Box 1 regarding the stringent role of symmetries concerning the allowed torque components. For example, when there is a two-fold rotation, it is clear there will be different torques pinned to the two perpendicular directions that we choose to be the x ad y axes, and in general, one would expect all torques to be defined by a 2×2 matrix. The presence of vertical mirror planes or in-plane rotational axes further halves the number of torque components.

Systems with three-fold rotational symmetry are the best examples to understand the emergence of novel torques upon symmetry breaking. To better appreciate this mechanism, let us focus on the torques that change sign with magnetization reversals of materials with the spacegroup P$\bar{3}$, which are the simplest to analyse although the result extends to the those with even dependence. These materials are centrosymmetric but lose this property and belong to the reduced P3 group when deposited onto a substrate. The remaining three-fold rotational symmetry then permits only two kinds of odd torques, one perpendicular and another parallel to the current. The trigonal structure which only maintains a single vertical mirror plane will then suppress the torque component parallel to the current. Similar ideas apply to the odd components of the torques. Therefore, the main message here is that

within a given class of crystals, new torques will appear when the interaction with the environment starts to disrupt internal crystalline symmetries. These new torque components will be superimposed onto the originally-existing ones that do not require symmetry breaking effects. Therefore, this superposition provides a unique way to control the characteristics of the torque by symmetry engineering of vdW materials. Another interesting result is that following this approach, we recover most of the synthetized 2D magnets such as CrI_3, $CrGeTe_3$ and Fe_3GeTe_2, but also some unexplored families such as the trihalides and the cubic magnets such as FeTe. In the same table we show the SOT directions allowed by the symmetries for all materials in the freestanding form (blue color) and under a substrate (red color). Most of the systems present inversion symmetry and as a result, do not show any torque in their freestanding form and require the presence of a substrate (modelled here by either removing the mirror plane parallel to the layer or the inversion operator out of the generating set). Interestingly, we also identify a set of materials with intrinsic crystal asymmetry leading to an intrinsic torque in Fe_3GeTe_2 ($P\bar{6}m2$) and certain magnetic trihalides like $CrBr_3$ ($P\bar{4}m2$)*, and magnetic Janus structures such as MnSTe ($P\bar{3}m1$)†. Additionally, we confirm that the angular dependence of this internally generated torque changes once the substrate is incorporated and breaks additional symmetries, with the only exception of the magnetic Janus TMD[168,169], for which the angular dependence remains the same.

Isotropic and anisotropic torques

Table 1

Repr. Mat.	Space Group	Crystal System	$\mathbf{H^e}$	$\mathbf{H^o}$
MX_3*	$P\bar{6}2m$ (189)	Hexagonal	$\tau_{\rm FL}\,\mathbf{J}\times\hat{\mathbf{z}}$	$\tau_{\rm DL}\,\mathbf{m}\times(\mathbf{J}\times\hat{\mathbf{z}})+\tau_z m_z\,\mathbf{J}+\tau_{\rm ani}\nabla_{\mathbf{m}}[\,J_y\,m_x m_y+J_x(m_y^2-m_x^2)/2]$
Fe_3GeTe_2*	$P\bar{6}m2$ (187)			$\tau_{\rm DL}\,\mathbf{m}\times(\mathbf{J}\times\hat{\mathbf{z}})+\tau_z m_z\,\mathbf{J}+\tau_{\rm ani}\nabla_{\mathbf{m}}[\,J_x\,m_x m_y+J_y(m_x^2-m_y^2)/2]$
$MnBi_2Te_2$	$P\bar{3}m1$ (164)	Trigonal	$\tau_{\rm FL}\,\mathbf{J}\times\hat{\mathbf{z}}$	$\tau_{\rm DL}\,\mathbf{m}\times(\mathbf{J}\times\hat{\mathbf{z}})+\tau_z m_z\,\mathbf{J}+\tau_{\rm ani}\nabla_{\mathbf{m}}[\,J_x\,m_x m_y+J_y(m_x^2-m_y^2)/2]$
MXY †	P3m1 (156)			
Fe_5GeTe_2	$R\bar{3}m$ (147)			
CrI_3	$P\bar{3}1m$ (162)			$\tau_{\rm DL}\,\mathbf{m}\times(\mathbf{J}\times\hat{\mathbf{z}})+\tau_z m_z\,\mathbf{J}+\tau_{\rm ani}\nabla_{\mathbf{m}}[\,J_y\,m_x m_y+J_x(m_y^2-m_x^2)/2]$
$CrGeTe_3$	$P\bar{3}$ (147)	Trigonal	$\tau^I_{\rm FL}\,\mathbf{J}\times\hat{\mathbf{z}}+\tau^{II}_F\,\mathbf{J}$	$\tau^I_{\rm DL}\,\mathbf{m}\times(\mathbf{J}\times\hat{\mathbf{z}})+\tau_z m_z\,\mathbf{J}+\tau^I_{\rm ani}\nabla_{\mathbf{m}}\left[J_y\,m_x m_y+\frac{J_x(m_x^2-m_y^2)}{2}\right]$ $+\tau^{II}_{\rm ani}\nabla_{\mathbf{m}}\left[J_y\,m_x m_y+\frac{J_x(m_x^2-m_y^2)}{2}\right]+\tau^{II}_o[(\mathbf{J}\times\boldsymbol{m})\cdot\hat{\boldsymbol{z}}]\hat{\boldsymbol{z}}$
FeTe †	P4/nmm (129)	Tetragonal	$\tau_{\rm FL}\,\mathbf{J}\times\hat{\mathbf{z}}$	$\tau_o\,\mathbf{m}\times(\mathbf{J}\times\hat{\mathbf{z}})+\tau_z m_z\,\mathbf{J}$
CrI_2	$P\bar{4}m2$ (115)	Orthorhombic	$\begin{pmatrix}0 & \tau^{xy}_{\rm FL}\\ \tau^{yx}_{\rm FL} & 0\end{pmatrix}\mathbf{J}$	$(\mathbf{M}\cdot\hat{\mathbf{z}})\begin{pmatrix}\tau^x_z & 0\\ 0 & \tau^y_z\end{pmatrix}\mathbf{J}+\mathbf{M}\cdot\begin{pmatrix}\tau^x_o & 0\\ 0 & \tau^y_o\end{pmatrix}\mathbf{J}\,\hat{\mathbf{z}}$
CrSBr	Pnmm (59)	Orthorhombic	$\begin{pmatrix}0 & \tau^{xy}_{\rm FL}\\ \tau^{yx}_{\rm FL} & 0\end{pmatrix}\mathbf{J}$	$(\mathbf{M}\cdot\hat{\mathbf{z}})\begin{pmatrix}\tau^x_z & 0\\ 0 & \tau^y_z\end{pmatrix}\mathbf{J}+\mathbf{M}\cdot\begin{pmatrix}\tau^x_o & 0\\ 0 & \tau^y_o\end{pmatrix}\mathbf{J}\,\hat{\mathbf{z}}$
$NiPS_3$	C2/m (12)	Monoclinic	$\begin{pmatrix}0 & \tau^{xy}_{\rm FL} & 0\\ \tau^{yx}_{\rm FL} & 0 & 0\\ 0 & \tau^{yz}_{\rm FL} & 0\end{pmatrix}\mathbf{J}$	$\begin{pmatrix}M_x\,\tau_o^{x,xx}+M_z\,\tau_o^{z,xx} & M_y\,\tau_o^{y,yx} & 0\\ M_y\,\tau_o^{y,xy} & M_x\,\tau_o^{x,yy}+M_z\,\tau_o^{z,yy} & 0\\ M_z\,\tau_o^{z,xz} & 0 & 0\end{pmatrix}\mathbf{J}+\mathbf{M}\cdot\begin{pmatrix}\tau_o^{xx} & 0 & 0\\ 0 & \tau_o^{yy} & 0\\ 0 & 0 & 0\end{pmatrix}\mathbf{J}\,\hat{\mathbf{z}}$

The Eqs.(1,2) allow us to consider the SOT as a phenomenon produced by a current-induced effective magnetic field prescribed by the symmetries and the SOC. However, despite the apparent simplicity of these expressions, the fields are function of both the magnetization direction and the applied current, and can take very complex functional forms, as is evident from the less symmetric materials reported in Table 1. Nevertheless, given that the functional form of the allowed torques in isotropic systems (like a 2D electron gas) resembles the one produced by the external effective magnetic given by $\mathbf{H}_{\rm eff}\propto\mathbf{J}\times\hat{z}$, early studies classified them in two components. These components are a field-like torque that produces magnetization precession and is characterized by the parameter $\tau_{\rm FL}$, and a damping-like torque that aligns the magnetization along the field direction and is proportional to $\tau_{\rm DL}$[170].

*Display intrinsic anisotropy-like SOT
†Display intrinsic field-like and damping-like SOT

These two torques define what we term isotropic torques

$$\mathbf{T}_{\text{iso}} = \mathbf{m} \times [\,\tau_{\text{FL}}\mathbf{J} \times \hat{\mathbf{z}} + \tau_{\text{DL}}\mathbf{m} \times (\mathbf{J} \times \hat{\mathbf{z}}) + \tau_{\text{z}}\text{m}_z\mathbf{J}\,], \tag{3}$$

given that the strength depends solely on the current magnitude J, allowing the definition of even and odd torques using a single parameter for each. Here, we use three parameters τ_{FL}, τ_{DL} and τ_{z} to represent the field strength for each symmetry. In fact, by following the procedure outlined in the Box 1, it is possible to show that such a simple description, where the torque is fully characterized by a single effective field, becomes characteristic of systems with two orthogonal vertical mirror planes, including totally isotropic systems. In the less symmetrical 2D systems without these two mirror planes, there will be a structural anisotropy between two orthogonal directions which would translate into an anisotropic electrical response. As a consequence, the current response will be characterized by the two diagonal elements of the conductivity tensor (σ_{xx} and σ_{yy}), while the torque response will be generally described by two or more effective magnetic fields. This means that the strength of the total torque will depend both on the current orientation and magnitude.

To better grasp these concepts, let us consider first the case of system possessing a three-fold rotational symmetry and at least a mirror plane (trigonal). In Box 1 we demonstrated how to compute the torque matrices for the C_{3v} point group symmetry and in Table 1 we combined it with Eq.(1) and Eq.(2) to express it in vectorial form, leading to Eq.(3). The first two torques are torques produced by the current-induced spin-polarization along $\mathbf{J} \times \hat{\mathbf{z}}$ with field-like and damping-like mechanisms respectively. Both are described by a single parameter indicating that the strength of the effective field does not depend on the current orientation. The last torque term is parallel to the current, becoming non-negligible only when there is an out-of-plane component of the magnetization m_z. When the mirror plane is removed, a novel field-like torque emerges that is perpendicular to both the current and the conventional field-like torque

$$\mathbf{T}_{\text{FL}}^{\text{ani}} = \mathbf{m} \times \left[\tau_{\text{FL}}^{I}\mathbf{J} \times \hat{\mathbf{z}} + \tau_{\text{FL}}^{II}\mathbf{J}\right]. \tag{4}$$

As a result, this acts as a superposition of two perpendicular in-plane effective magnetic fields and thus leads to an anisotropic response as a function of the current direction.

Lower symmetrical systems, such as those with two-fold rotational symmetry, possess a structural anisotropy between two orthogonal crystalline directions. Therefore, the most general relation between the current and the torques should appear in the form of a 2×2 matrix, which is indeed the case reported in Table 1,

$$\mathbf{T}_{\text{FL}}^{\text{ani}} = \mathbf{m} \times \begin{pmatrix} 0 & \tau_{\text{FL}}^{yx} \\ \tau_{\text{FL}}^{xy} & 0 \end{pmatrix} \mathbf{J} \tag{5}$$

where τ_{FL}^{yx} and τ_{FL}^{xy} two independent parameters. Since this field is invariant against two-fold rotation, it is fundamentally different to that in Eq. (4). For example, for $\tau_{\text{FL}}^{xy} = 0$, the field will vanish if the current is applied in the y direction, which will not happen for systems with three-fold symmetry. Therefore, it is evident here that the existence of two-parameters will change the effective field strength with the current direction enabling a general case of anisotropic torques.

Other systems such as Fe_3GeTe_2 do not have inversion symmetry due to the lack of two orthogonal mirror planes. In these systems, the spin-orbit interaction allows for a SOT that behaves similarly to the one produced by a magnetic anisotropy. The axis of the anisotropy is defined by the remaining mirror axis and the direction of the current. It is similar to a magnetic anisotropy in the sense that one can associate the following energy density[154]

$$E_{\text{AL}} = J_x m_x m_y - \frac{1}{2} J_y (m_x^2 - m_y^2), \tag{6}$$

which is quadratic in $\mathbf{m}$, and it produces the effective torque through its gradient with respect to the magnetization $\mathbf{T}_{\text{AL}} = -\tau_{\text{AL}} \boldsymbol{\nabla}_{\mathbf{m}} E_{\text{AL}}$.

Certain systems such as monoclinic crystals with just one mirror axis and a two-fold rotation, facilitate the formation of torques possessing components from effective magnetic field proportionals to $\mathbf{J} \times \hat{\mathbf{y}}$ and $\mathbf{J} \times \hat{\mathbf{x}}$, which are favorable conditions for switching magnets with an out-of-plane perpendicular magnetic anisotropy.

Comparison to experiments

Experimentally, we are able to detect these predicted torques via low-frequency second-harmonic measurements[171] and current-induced FMR experiments[131,172]. In both detection schemes, we can consider the current-induced

effective fields that tilt the static magnetization direction by a free energy change of $\mathbf{M}\cdot\mathbf{H}_{\mathrm{SOC}}$, or that drive magnetic precession with a magnetic torque of $\mathbf{M}\times\mathbf{H}_{\mathrm{SOC}}$. We can substitute the vector expressions of $\mathbf{H}_{\mathrm{SOC}}$ fields in Table 1 to predict the torque symmetry for future magnetization-control experiments. For example, by using $\mathbf{J}\times\hat{\mathbf{z}}$ as $\mathbf{H}_{\mathrm{SOC}}$, we have the torque expression of $\mathbf{M}\times(\mathbf{J}\times\hat{\mathbf{z}})$ for spin dynamics excitation. Assuming that a driving current is flowing along the x direction, such that $\mathbf{J}\parallel\hat{\mathbf{x}}$, the torque expression reduces into $\mathbf{M}\times\hat{\mathbf{y}}$. This suggests that FMR amplitudes excited by this $\mathbf{H}_{\mathrm{SOC}}$ display $\cos\phi$ dependence when the magnetization is rotated in-plane with ϕ defined by the angle between $\mathbf{J}$ and $\mathbf{M}$. In general, measured FMR voltages also have $\sin 2\phi$ dependence due to a time-dependent change of resistance arising from anisotropic magnetoresistance and magnetic precession[173]. As a result, we expect $\mathbf{H}_{\mathrm{SOC}}(\propto\mathbf{J}\times\hat{\mathbf{z}})$ produces $\sin 2\phi\cos\phi$ dependence when we perform FMR voltage measurements for in-plane angle rotation of $\mathbf{M}$. We can apply the same vector analysis for other effective fields for FMR experiments as well as the low-frequency second-harmonic experiments.

Strength of the torques

An important point for comparison with experimental data is how to obtain theoretically the strength of the SOT parameters. In 2D materials, the SOT originates solely from the current-induced spin density in the material. Therefore, in the limit of small currents, the best approach to compute these parameters is via the Kubo formula within the linear-response approximation[174]. This approach requires knowledge of the magnetization-dependent Hamiltonian $H(\mathbf{m})$ and an effective way to compute its associated retarded Green's functions $G^{+}(H,E)$. For non-interacting electrons, the spin-orbit torque is determined by the following expression

$$\mathbf{T}^{\alpha}(\mu,T)=-\frac{2\pi\Delta_{\mathrm{ex}}\mathrm{J}_{\alpha}}{\sigma_{\alpha\alpha}}\int dE\,f(E-\mu,T)\,\mathrm{Im}\mathrm{Tr}\left[\mathrm{Im}G^{+}\hat{\mathrm{J}}_{\alpha}\frac{dG^{+}}{dE}(\hat{\boldsymbol{\sigma}}\times\mathbf{m})\right], \tag{7}$$

where Im Tr represents the imaginary part of the trace of the operators in the brackets, $f(E-\mu,T)$ the Fermi-Dirac distribution for a given chemical potential μ and temperature T, $\hat{\mathbf{J}}$ the current-density operator and $\mathbf{J}$ its macroscopic average, $\sigma_{\alpha\alpha}$ the conductivity, and $\hat{\boldsymbol{\sigma}}$ the Pauli matrices operator. This approach gives access to the SOTs by making no assumptions on their dependence against magnetization. Furthermore, Eq. (7) can be further sliced into two contributions, those resulting from scattering mechanisms of electrons at the Fermi level (proportional to the conductivity), and those arising from a Fermi-sea contribution, which in principle can provide both dissipative and non-dissipative SOTs, and are primarily scattering independent contributions[11]. The existence of a SOT proportional to scattering times also evidences that disorder plays a major role to determine the system's behavior. In simple systems, the Kubo formula can be evaluated following semi-analytic solutions based on perturbation theory[175,176], where the disorder is usually described by point impurities. For low concentration of impurities and when the single scattering approximation is valid, the Kubo formula reduces to the Boltzmann equation, which offers a simple way to estimate the behavior of the torque parameters[170]. However, a quantitative determination for a generic disorder or a structurally complex system is only attainable through linear scaling quantum transport methodologies[174], that enable reaching the required size scales to study the torques in the diffusive and localized regimes. For ferromagnetic materials, the magnetization can be instead replaced by the exchange-correlation field, facilitating the use of the Kubo formula to determine the torques from first principles simulations[177,178]. Beyond the Kubo formula, nonadiabatic time-dependent evolution in realistic systems is also a great challenge, although there are some recent efforts along this direction[179].

The Kubo formula provides a method to compute the torque parameters in units of a torque density ($\mathrm{eV/m^3}$). However, since these parameters depend directly on the driven current density, a current-to-torque conversion efficiency is usually defined. Such an efficiency definition is quite straightforward in systems where the torque is mostly due to the spin Hall effect, so it can be connected to the spin Hall angle which is given by the ratio between the spin and charge conductivities[11]. Following similar considerations, the torque conductivity σ_{τ} can be defined as the angular momentum absorbed by the magnet per second per unit interface area per unit applied electric field[156], from which the torque efficiency χ_{α}^{X} is derived as:

$$\chi_{\alpha}^{X}\equiv\frac{2e}{\hbar}\frac{M_s t}{\gamma}\frac{\tau_X}{\mathrm{J}_{\alpha}}, \tag{8}$$

where M_s the saturation magnetization, X the torque label (FL,DL, etc), t the thickness of the magnet, which is taken as the Van der Waal gap in 2D materials. The former expression defines an efficiency for different kind of torques classified according to their symmetries, but there is an alternative dimensionless expression which describes the

efficiency according to the torque's directions expressed as[139]

$$\chi_{\alpha\beta} \equiv \frac{e\Delta_{\rm ex} t}{\hbar}\frac{\mathrm{T}_\beta}{\mathrm{J}_\alpha}. \tag{9}$$

Both expressions allow to quantify a torque efficiency due to a source of spins independently of geometric factors. For a Cobalt/Platinum system $\chi_\alpha \approx 0.0075$ for a $t \approx 0.85$ nm[180], while in experiments considering TMD/Py heterostructures the efficiency only reaches values between $10^{-5} - 10^{-3}$ [162]. Another important parameter is given by $\chi_\alpha^X/\chi_\alpha^{\rm FL} = \tau_{\rm X}/\tau_{\rm FL}$ which measures the relative value of all torques against the dissipative field-like contribution and generally ranges from 1-10. Notice that in 2D materials $\mathrm{M}_s t$ is actually the magnetization per unit area or sheet magnetization[107]. From all this discussion, it becomes clear that a lot of work remains to be done to obtain realistic and quantitative information about spin torque efficiency in vdW heterostructures combining 2D magnets with strong SOC materials. Beyond well-controlled ab-initio simulations and the elaboration of properly designed SOC-dependent tight-binding models, the use of computational methodologies that can numerically solve the Kubo formula Eq. (7) for large scale models is a grand challenge, particularly when disorder effects affecting the spin physics demand non-perturbative treatments. Brute-force simulations using linear scaling methods demand further developments and implementations, as well as comparison of their predictions with future experiments.

As a final remark, the spin-Hall effect[11] should exist in a variety of vdW material systems, both magnetic and non-magnetic, except in the single monolayer limit. In order to exploit such spin-charge phenomena, vdW heterostructures are usually fabricated with one magnetic layer in direct contact with a spin current source, so as to have a close and efficient magnetization manipulation. The symmetry of spin-Hall effect is well-established and the spin-current source layer could be also magnetic, in which case additional magnetization-dependent anomalous components[181–183] might appear.

Outlook

There are many possibilities of creating new hybrid materials with emerging spin-dependent interface properties[184]. Among the vast zoo of novel structures, theory and modelling based on symmetry features of interfaces bring a pathfinder to find the most suitable conditions for best controlling spin transport through spin-orbit or exchange coupling fields. One most urgent quest is the search for the upper limit of the achievable spin-orbit torque efficiency (at RT and with scalable materials), which could ultimately enable low-energy and fast switching of the material magnetization in the frame of SOT memory technologies[5,10,120,185]. Such is a challenging task which will require a combination of theoretical and experimental research within a large community of material growers, using advanced characterization and simulation tools and optimizing device fabrication approaches. The search for materials with high Curie or Néel temperatures is also a key aspect of this research, and efforts to guide experiments such as the recently studied monolayer Fe_3P with predicted T_C of 420 K[186] should be followed. In this regard, varying the exchange coupling strength by controlling molecular orbital alignments in 2D magnetic semiconductors[53] could be an interesting approach where $CrWI_6$ and $CrWGe_2Te_6$ are predicted to display ferromagnetic order above RT via the purely super-exchange interaction. Furthermore, high-throughput computation screening using an existing materials database[187] and other material informatics methods could be an effective approach to guide us towards discoveries of novel high-T_C vdW magnetic materials.

Here we have focused our attention to the more familiar ferromagnetic cases, but this approach is valid for predicting torques in non-magnetic vdW systems by using the same space group analysis as well as for novel types of torques in antiferromagnetic systems, such as the Néel SOT[188] and other antiferromagnetic specific SOC effects[189]. Looking further for more exotic 2D vdW materials with order parameters, multiferroics is predicted in a certain class of 2D materials[190] such as in a doped $CrBr_3$ monolayer[191], in a bilayer of halogen-intercalated phosphorene[192] as well as in a monolayer $ReWCl_6$ with magnetic transitions induced by electric field[193]. Some vdW magnetic materials, such as $MnBi_2Te_4$[194–196], host topological electronic states and offer unique topologically-protected transport phenomena[197]. We anticipate that this research domain will be rapidly expanding to explore the topological transport as well as its use in spintronic applications[198]. Additionally, nontrivial spin transport physics is also expected to develop at complex interfaces of vdW heterostructures, including the generation of skyrmions[199–201], the excitation and detection of magnons at the 2D limit[202–204] and their interaction with other spin-dependent characteristics of interfaced materials[184]. Furthermore, proximity effects could reveal unprecedented manifestations of entanglement and many-body physics, as recently discussed in the context of topological superconductivity or unconventional ferroelectricity in magic-angle twisted bi/trilayer graphene and related moiré superlattices[205,206]. There remains a lot to be explored for spin transport at the frontier of layered magnetism and SOC materials, and likely many exciting discoveries waiting to emerge.

References

1. Huang, B. *et al.* Layer-dependent ferromagnetism in a van der Waals crystal down to the monolayer limit. *Nature* **546**, 270–273, DOI: 10.1038/nature22391 (2017).
2. Hirohata, A. *et al.* Review on spintronics: Principles and device applications. *J. Magn. Magn. Mater.* **509**, 166711, DOI: https://doi.org/10.1016/j.jmmm.2020.166711 (2020).
3. Grollier, J. *et al.* Neuromorphic spintronics. *Nat. Electron.* **3**, 360–370, DOI: 10.1038/s41928-019-0360-9 (2020).
4. Lin, X., Yang, W., Wang, K. L. & Zhao, W. Two-dimensional spintronics for low-power electronics. *Nat. Electron.* **2**, 274–283, DOI: 10.1038/s41928-019-0273-7 (2019).
5. Kawahara, T., Ito, K., Takemura, R. & Ohno, H. Spin-transfer torque ram technology: Review and prospect. *Microelectron. Reliab.* **52**, 613–627, DOI: https://doi.org/10.1016/j.microrel.2011.09.028 (2012). Advances in non-volatile memory technology.
6. Bhatti, S. *et al.* Spintronics based random access memory: a review. *Mater. Today* **20**, 530–548, DOI: https://doi.org/10.1016/j.mattod.2017.07.007 (2017).
7. Chernyshov, A. *et al.* Evidence for reversible control of magnetization in a ferromagnetic material by means of spin–orbit magnetic field. *Nat. Phys.* **5**, 656–659, DOI: 10.1038/nphys1362 (2009). 0812.3160.
8. Miron, I. M. *et al.* Perpendicular switching of a single ferromagnetic layer induced by in-plane current injection. *Nature* **476**, 189–193, DOI: 10.1038/nature10309 (2011).
9. Liu, L. *et al.* Spin-Torque Switching with the Giant Spin Hall Effect of Tantalum. *Science* **336**, 555–558, DOI: 10.1126/science.1218197 (2012). 1203.2875.
10. Cubukcu, M. *et al.* Ultra-Fast Perpendicular Spin-Orbit Torque MRAM. *IEEE Transactions on Magn.* **54**, 9300204, DOI: 10.1109/TMAG.2017.2772185 (2018). 1509.02375.
11. Sinova, J., Valenzuela, S. O., Wunderlich, J., Back, C. H. & Jungwirth, T. Spin Hall effects. *Rev. Mod. Phys.* **87**, 1213–1260, DOI: 10.1103/RevModPhys.87.1213 (2015).
12. Edelstein, V. M. Spin polarization of conduction electrons induced by electric current in two-dimensional asymmetric electron systems. *Solid State Commun.* **73**, 233–235, DOI: 10.1016/0038-1098(90)90963-C (1990).
13. Manchon, A. *et al.* Current-induced spin-orbit torques in ferromagnetic and antiferromagnetic systems. *Rev. Mod. Phys.* **91**, 035004, DOI: 10.1103/RevModPhys.91.035004 (2019). 1801.09636.
14. Gong, C. *et al.* Discovery of intrinsic ferromagnetism in two-dimensional van der Waals crystals. *Nature* **546**, 265–269, DOI: 10.1038/nature22060 (2017).
15. Burch, K. S., Mandrus, D. & Park, J. G. Magnetism in two-dimensional van der Waals materials. *Nature* **563**, 47–52, DOI: 10.1038/s41586-018-0631-z (2018).
16. Fei, Z. *et al.* Two-dimensional itinerant ferromagnetism in atomically thin Fe_3GeTe_2. *Nat. Mater.* **17**, 778–782, DOI: 10.1038/s41563-018-0149-7 (2018).
17. Li, H., Ruan, S. & Zeng, Y. J. Intrinsic Van Der Waals Magnetic Materials from Bulk to the 2D Limit: New Frontiers of Spintronics. *Adv. Mater.* **31**, 1–34, DOI: 10.1002/adma.201900065 (2019).
18. Gong, Y. *et al.* Experimental Realization of an Intrinsic Magnetic Topological Insulator *. *Chin. Phys. Lett.* **36**, 076801, DOI: 10.1088/0256-307X/36/7/076801 (2019).
19. Geim, A. K. & Grigorieva, I. V. Van der waals heterostructures. *Nature* **499**, 419–425, DOI: 10.1038/nature12385 (2013).
20. Liu, Y. *et al.* Van der waals heterostructures and devices. *Nat. Rev. Mater.* **1**, 16042, DOI: 10.1038/natrevmats.2016.42 (2016).
21. Andrei, E. Y. *et al.* The marvels of moiré materials. *Nat. Rev. Mater.* **6**, 201–206, DOI: 10.1038/s41578-021-00284-1 (2021).
22. Freitas, D. C. *et al.* Ferromagnetism in layered metastable 1T-$CrTe_2$. *J. Phys. Condens. Matter* **27**, 176002, DOI: 10.1088/0953-8984/27/17/176002 (2015).
23. Freitas, D. C. *et al.* Antiferromagnetism and ferromagnetism in layered 1T-$CrSe_2$ with v and Ti replacements. *Phys. Rev. B - Condens. Matter Mater. Phys.* **87**, 014420, DOI: 10.1103/PhysRevB.87.014420 (2013).

24. Zhang, W.-B., Qu, Q., Zhu, P. & Lam, C.-H. Robust intrinsic ferromagnetism and half semiconductivity in stable two-dimensional single-layer chromium trihalides. *J. Mater. Chem. C* **3**, 12457–12468, DOI: 10.1039/C5TC02840J (2015). 1507.07275.

25. McGuire, M. A., Dixit, H., Cooper, V. R. & Sales, B. C. Coupling of Crystal Structure and Magnetism in the Layered, Ferromagnetic Insulator CrI_3. *Chem. Mater.* **27**, 612–620, DOI: 10.1021/cm504242t (2015).

26. McGuire, M. A. *et al.* Magnetic behavior and spin-lattice coupling in cleavable van der Waals layered $CrCl_3$ crystals. *Phys. Rev. Mater.* **1**, 14001, DOI: 10.1103/PhysRevMaterials.1.014001 (2017).

27. Joy, P. A. & Vasudevan, S. Magnetism in the layered transition-metal thiophosphates MPS_3 (M=Mn, Fe, and Ni). *Phys. Rev. B* **46**, 5425–5433, DOI: 10.1103/PhysRevB.46.5425 (1992).

28. Lin, W., Chen, K., Zhang, S. & Chien, C. L. Enhancement of Thermally Injected Spin Current through an Antiferromagnetic Insulator. *Phys. Rev. Lett.* **116**, 186601, DOI: 10.1103/PhysRevLett.116.186601 (2016). 1603.00931.

29. Bonilla, M. *et al.* Strong room-temperature ferromagnetism in VSe_2 monolayers on van der Waals substrates. *Nat. Nanotechnol.* **13**, 289–293, DOI: 10.1038/s41565-018-0063-9 (2018).

30. Deng, Y. *et al.* Gate-tunable room-temperature ferromagnetism in two-dimensional Fe_3GeTe_2. *Nature* **563**, 94–99, DOI: 10.1038/s41586-018-0626-9 (2018).

31. O'Hara, D. J. *et al.* Room Temperature Intrinsic Ferromagnetism in Epitaxial Manganese Selenide Films in the Monolayer Limit. *Nano Lett.* **18**, 3125–3131, DOI: 10.1021/acs.nanolett.8b00683 (2018). 1802.08152.

32. O'Hara, D. J., Zhu, T. & Kawakami, R. K. Importance of Paramagnetic Background Subtraction for Determining the Magnetic Moment in Epitaxially Grown Ultrathin van der Waals Magnets. *IEEE Magn. Lett.* **9**, 1–5, DOI: 10.1109/LMAG.2018.2867339 (2018).

33. Walker, M. B. & Withers, R. L. Stacking of charge-density waves in 1T transition-metal dichalcogenides. *Phys. Rev. B* **28**, 2766–2774, DOI: 10.1103/PhysRevB.28.2766 (1983).

34. Eaglesham, D. J., Withers, R. L. & Bird, D. M. Charge-density-wave transitions in 1T-VSe_2. *J. Phys. C: Solid State Phys.* **19**, 359–367, DOI: 10.1088/0022-3719/19/3/006 (1986).

35. Feng, J. *et al.* Electronic Structure and Enhanced Charge-Density Wave Order of Monolayer VSe_2. *Nano Lett.* **18**, 4493–4499, DOI: 10.1021/acs.nanolett.8b01649 (2018).

36. Yang, J. *et al.* Thickness dependence of the charge-density-wave transition temperature in VSe_2. *Appl. Phys. Lett.* **105**, 063109, DOI: 10.1063/1.4893027 (2014).

37. Coelho, P. M. *et al.* Charge Density Wave State Suppresses Ferromagnetic Ordering in VSe_2 Monolayers. *The J. Phys. Chem. C* **123**, 14089–14096, DOI: 10.1021/acs.jpcc.9b04281 (2019).

38. Burch, K. S., Mandrus, D. & Park, J.-G. Magnetism in two-dimensional van der waals materials. *Nature* **563**, 47–52, DOI: 10.1038/s41586-018-0631-z (2018).

39. Gibertini, M., Koperski, M., Morpurgo, A. F. & Novoselov, K. S. Magnetic 2d materials and heterostructures. *Nat. Nanotechnol.* **14**, 408–419, DOI: 10.1038/s41565-019-0438-6 (2019).

40. Gong, C. & Zhang, X. Two-dimensional magnetic crystals and emergent heterostructure devices. *Science* **363**, DOI: 10.1126/science.aav4450 (2019). https://science.sciencemag.org/content/363/6428/eaav4450.full.pdf.

41. Mak, K. F., Shan, J. & Ralph, D. C. Probing and controlling magnetic states in 2d layered magnetic materials. *Nat. Rev. Phys.* **1**, 646–661, DOI: 10.1038/s42254-019-0110-y (2019).

42. Huang, B. *et al.* Emergent phenomena and proximity effects in two-dimensional magnets and heterostructures. *Nat. Mater.* **19**, 1276–1289, DOI: 10.1038/s41563-020-0791-8 (2020).

43. Huang, P. *et al.* Recent advances in two-dimensional ferromagnetism: materials synthesis, physical properties and device applications. *Nanoscale* **12**, 2309–2327, DOI: 10.1039/C9NR08890C (2020).

44. Wei, S. *et al.* Emerging intrinsic magnetism in two-dimensional materials: theory and applications. *2D Mater.* **8**, 012005, DOI: 10.1088/2053-1583/abc8cb (2020).

45. Han, W. Perspectives for spintronics in 2d materials. *APL Mater.* **4**, 032401, DOI: 10.1063/1.4941712 (2016). https://doi.org/10.1063/1.4941712.

46. Avsar, A. *et al.* Colloquium: Spintronics in graphene and other two-dimensional materials. *Rev. Mod. Phys.* **92**, 021003, DOI: 10.1103/RevModPhys.92.021003 (2020).

47. Husain, S. *et al.* Emergence of spinâ€“orbit torques in 2d transition metal dichalcogenides: A status update. *Appl. Phys. Rev.* **7**, 041312, DOI: 10.1063/5.0025318 (2020). https://doi.org/10.1063/5.0025318.

48. Ahn, E. C. 2d materials for spintronic devices. *npj 2D Mater. Appl.* **4**, 17, DOI: 10.1038/s41699-020-0152-0 (2020).

49. Anderson, P. W. Antiferromagnetism. Theory of superexchange interaction. *Phys. Rev.* **79**, 350–356, DOI: 10.1103/PhysRev.79.350 (1950).

50. Lado, J. L. & Fernández-Rossier, J. On the origin of magnetic anisotropy in two dimensional CrI_3. *2D Mater.* **4**, 35002, DOI: 10.1088/2053-1583/aa75ed (2017). 1704.03849.

51. Kanamori, J. Superexchange interaction and symmetry properties of electron orbitals. *J. Phys. Chem. Solids* **10**, 87–98, DOI: 10.1016/0022-3697(59)90061-7 (1959).

52. Goodenough, J. B. Theory of the role of covalence in the perovskite-type manganites [La,M(II)]MnO_3. *Phys. Rev.* **100**, 564–573, DOI: 10.1103/PhysRev.100.564 (1955).

53. Huang, C. *et al.* Toward Intrinsic Room-Temperature Ferromagnetism in Two-Dimensional Semiconductors. *J. Am. Chem. Soc.* **140**, 11519–11525, DOI: 10.1021/jacs.8b07879 (2018).

54. Kim, H. H. *et al.* Evolution of interlayer and intralayer magnetism in three atomically thin chromium trihalides. *Proc. Natl. Acad. Sci. United States Am.* **166**, 11131–11136, DOI: 10.1073/pnas.1902100116 (2019). 1903.01409.

55. Wang, F. *et al.* New Frontiers on van der Waals Layered Metal Phosphorous Trichalcogenides. *Adv. Funct. Mater.* **28**, 1802151, DOI: 10.1002/adfm.201802151 (2018).

56. Ur Rehman, Z. *et al.* Magnetic isotropy/anisotropy in layered metal phosphorous Trichalcogenide MPS_3 (M = Mn, Fe)single crystals. *Micromachines* **9**, DOI: 10.3390/mi9060292 (2018).

57. Kim, K. *et al.* Suppression of magnetic ordering in XXZ-type antiferromagnetic monolayer $NiPS_3$. *Nat. Commun.* **10**, 345, DOI: 10.1038/s41467-018-08284-6 (2019).

58. Zener, C. Interaction between the d-shells in the transition metals. II. Ferromagnetic compounds of manganese with Perovskite structure. *Phys. Rev.* **82**, 403–405, DOI: 10.1103/PhysRev.82.403 (1951).

59. Jonker, G. & Van Santen, J. Ferromagnetic compounds of manganese with perovskite structure. *Physica* **16**, 337–349, DOI: 10.1016/0031-8914(50)90033-4 (1950).

60. Wang, N. *et al.* Transition from ferromagnetic semiconductor to ferromagnetic metal with enhanced curie temperature in $cr_2ge_2te_6$ via organic ion intercalation. *J. Am. Chem. Soc.* **141**, 17166–17173, DOI: 10.1021/jacs.9b06929 (2019). PMID: 31599579, https://doi.org/10.1021/jacs.9b06929.

61. Verzhbitskiy, I. A. *et al.* Controlling the magnetic anisotropy in $Cr_2Ge_2Te_6$ by electrostatic gating. *Nat. Electron.* **3**, 460–465, DOI: 10.1038/s41928-020-0427-7 (2020).

62. Cai, X. *et al.* Atomically thin $CrCl_3$: an in-plane layered antiferromagnetic insulator. *Nano letters* **19**, 3993–3998 (2019).

63. Wiedenmann, A., Rossat-Mignod, J., Louisy, A., Brec, R. & Rouxel, J. Neutron diffraction study of the layered compounds $MnPSe_3$ and $FePSe_3$. *Solid State Commun.* **40**, 1067–1072 (1981).

64. Long, G. *et al.* Isolation and characterization of few-layer manganese thiophosphite. *ACS nano* **11**, 11330–11336 (2017).

65. Le Flem, G., Brec, R., Ouvard, G., Louisy, A. & Segransan, P. Magnetic interactions in the layer compounds MPX_3 (M= Mn, Fe, Ni; X= S, Se). *J. Phys. Chem. Solids* **43**, 455–461 (1982).

66. Ghazaryan, D. *et al.* Magnon-assisted tunnelling in van der waals heterostructures based on $CrBr_3$. *Nat. Electron.* **1**, 344–349 (2018).

67. Samuelsen, E., Silberglitt, R., Shirane, G. & Remeika, J. Spin waves in ferromagnetic $CrBr_3$ studied by inelastic neutron scattering. *Phys. Rev. B* **3**, 157 (1971).

68. Lee, J.-U. *et al.* Ising-type magnetic ordering in atomically thin $FePS_3$. *Nano letters* **16**, 7433–7438 (2016).

69. Liu, P. *et al.* Exploring the magnetic ordering in atomically thin antiferromagnetic $MnPSe_3$ by raman spectroscopy. *J. Alloy. Compd.* **828**, 154432 (2020).

70. Huang, B. *et al.* Electrical control of 2D magnetism in bilayer CrI_3. *Nat. Nanotechnol.* **13**, 544–548, DOI: 10.1038/s41565-018-0121-3 (2018). 1802.06979.

71. Zhong, D. *et al.* Van der waals engineering of ferromagnetic semiconductor heterostructures for spin and valleytronics. *Sci. advances* **3**, e1603113 (2017).

72. Chattopadhyay, T., Brückel, T. & Burlet, P. Spin correlation in the frustrated antiferromagnet MnS_2 above the néel temperature. *Phys. Rev. B* **44**, 7394 (1991).

73. Son, S. *et al.* Bulk properties of the van der Waals hard ferromagnet VI_3. *Phys. Rev. B* **99**, 41402, DOI: 10.1103/PhysRevB.99.041402 (2019). 1812.05284.

74. Khan, S. *et al.* Spin dynamics study in layered van der waals single-crystal $Cr_2Ge_2Te_6$. *Phys. Rev. B* **100**, 134437 (2019).

75. Lin, M.-W. *et al.* Ultrathin nanosheets of $CrSiTe_3$: a semiconducting two-dimensional ferromagnetic material. *J. Mater. Chem. C* **4**, 315–322, DOI: 10.1039/C5TC03463A (2016).

76. McGuire, M. A. *et al.* Antiferromagnetism in the van der Waals layered spin-lozenge semiconductor $CrTe_3$. *Phys. Rev. B* **95**, 144421, DOI: 10.1103/PhysRevB.95.144421 (2017). 1701.08621.

77. Lv, H., Lu, W., Shao, D., Liu, Y. & Sun, Y. Strain-controlled switch between ferromagnetism and antiferromagnetism in 1T-CrX_2 (X= Se, Te) monolayers. *Phys. Rev. B* **92**, 214419 (2015).

78. Sun, X. *et al.* Room temperature ferromagnetism in ultra-thin van der waals crystals of 1T-$CrTe_2$. *Nano Res.* **13**, 3358–3363 (2020).

79. Chu, J. *et al.* Sub-millimeter-scale growth of one-unit-cell-thick ferrimagnetic Cr_2S_3 nanosheets. *Nano letters* **19**, 2154–2161 (2019).

80. Xie, L. *et al.* An atomically thin air-stable narrow-gap semiconductor Cr_2S_3 for broadband photodetection with high responsivity. *Adv. Electron. Mater.* 2000962 (2020).

81. Zeugner, A. *et al.* Chemical aspects of the candidate antiferromagnetic topological insulator $MnBi_2Te_4$. *Chem. Mater.* **31**, 2795–2806 (2019).

82. Kan, M., Adhikari, S. & Sun, Q. Ferromagnetism in MnX_2 (X= S, Se) monolayers. *Phys. Chem. Chem. Phys.* **16**, 4990–4994 (2014).

83. Itoh, H. & Miyahara, S. Magnetic susceptibility and thermal expansion of $MnSe_2$ with pyrite structure. *J. Phys. Soc. Jpn.* **42**, 470–472 (1977).

84. Lei, S. *et al.* High mobility in a van der waals layered antiferromagnetic metal. *Sci. advances* **6**, eaay6407 (2020).

85. Nakano, M. *et al.* Intrinsic 2D Ferromagnetism in V_5Se_8 Epitaxial Thin Films. *Nano Lett.* **19**, 8806–8810, DOI: 10.1021/acs.nanolett.9b03614 (2019).

86. Morosan, E. *et al.* Sharp switching of the magnetization in $Fe_{0.25}TaS_2$. *Phys. Rev. B* **75**, 104401, DOI: 10.1103/PhysRevB.75.104401 (2007).

87. Zhang, Y. *et al.* Ultrathin magnetic 2d single-crystal CrSe. *Adv. Mater.* **31**, 1900056 (2019).

88. Zhang, H., Liu, L.-M. & Lau, W.-M. Dimension-dependent phase transition and magnetic properties of VS_2. *J. Mater. Chem. A* **1**, 10821–10828 (2013).

89. Zhang, L.-Z. *et al.* Critical behavior and magnetocaloric effect of the quasi-two-dimensional room-temperature ferromagnet Cr_4Te_5. *Phys. Rev. B* **101**, 214413 (2020).

90. Liu, Y. *et al.* Magnetic anisotropy and entropy change in trigonal Cr_5Te_8. *Phys. Rev. B* **100**, 245114 (2019).

91. Seo, J. *et al.* Nearly room temperature ferromagnetism in a magnetic metal-rich van der waals metal. *Sci. advances* **6**, eaay8912 (2020).

92. May, A. F. *et al.* Ferromagnetism Near Room Temperature in the Cleavable van der Waals Crystal Fe_5GeTe_2. *ACS Nano* **13**, 4436–4442, DOI: 10.1021/acsnano.8b09660 (2019).

93. Zhuang, H. L., Kent, P. R. & Hennig, R. G. Strong anisotropy and magnetostriction in the two-dimensional Stoner ferromagnet Fe_3GeTe_2. *Phys. Rev. B* **93**, 134407, DOI: 10.1103/PhysRevB.93.134407 (2016).

94. Blundell, S. & Thouless, D. *Magnetism in Condensed Matter*, vol. 71 of *Oxford master series in condensed matter physics* (Oxford University Press, Oxford, 2003).

95. Weiss, P. L'hypothèse du champ moléculaire et la propriété ferromagnétique. *J. de Physique Théorique et Appliquée* **6**, 661–690, DOI: 10.1051/jphystap:019070060066100 (1907).

96. Watanabe, H. Collective Electron Ferromagnetism, II. *J. Phys. Soc. Jpn.* **3**, 317–322, DOI: 10.1143/JPSJ.3.317 (1948).

97. Stoner, E. C. Collective electron ferromagnetism II. Energy and specific heat. *Proc. Royal Soc. London. Ser. A. Math. Phys. Sci.* **169**, 339–371, DOI: 10.1098/rspa.1939.0003 (1939).

98. May, A. F., Calder, S., Cantoni, C., Cao, H. & McGuire, M. A. Magnetic structure and phase stability of the van der Waals bonded ferromagnet $Fe_{3-x}GeTe_2$. *Phys. Rev. B* **93**, 14411, DOI: 10.1103/PhysRevB.93.014411 (2016). 1508.06959.

99. Wang, Y. *et al.* Magnetic anisotropy and topological Hall effect in the trigonal chromium tellurides Cr_5Te_8. *Phys. Rev. B* **100**, 24434, DOI: 10.1103/PhysRevB.100.024434 (2019).

100. Yan, J. *et al.* Anomalous hall effect of the quasi-two-dimensional weak itinerant ferromagnet cr 4.14 te 8. *EPL (Europhysics Lett.* **124**, 67005, DOI: 10.1209/0295-5075/124/67005 (2019).

101. Mermin, N. D. & Wagner, H. Absence of ferromagnetism or antiferromagnetism in one- or two-dimensional isotropic Heisenberg models. *Phys. Rev. Lett.* **17**, 1133–1136, DOI: 10.1103/PhysRevLett.17.1133 (1966).

102. Jiang, S., Li, L., Wang, Z., Mak, K. F. & Shan, J. Controlling magnetism in 2d cri_3 by electrostatic doping. *Nat. Nanotechnol.* **13**, 549–553, DOI: 10.1038/s41565-018-0135-x (2018).

103. Song, T. *et al.* Switching 2D magnetic states via pressure tuning of layer stacking. *Nat. Mater.* **18**, 1298–1302, DOI: 10.1038/s41563-019-0505-2 (2019). 1905.10860.

104. Matsukura, F., Tokura, Y. & Ohno, H. Control of magnetism by electric fields. *Nat. Nanotechnol.* **10**, 209–220, DOI: 10.1038/nnano.2015.22 (2015).

105. McGuire, M. A. Crystal and magnetic structures in layered, transition metal dihalides and trihalides. *Crystals* **7**, DOI: 10.3390/cryst7050121 (2017). 1704.08225.

106. Sivadas, N., Okamoto, S. & Xiao, D. Gate-Controllable Magneto-optic Kerr Effect in Layered Collinear Antiferromagnets. *Phys. Rev. Lett.* **117**, 267203, DOI: 10.1103/PhysRevLett.117.267203 (2016). 1607.02156.

107. Jiang, S., Shan, J. & Mak, K. F. Electric-field switching of two-dimensional van der Waals magnets. *Nat. Mater.* **17**, 406–410, DOI: 10.1038/s41563-018-0040-6 (2018).

108. Song, T. *et al.* Voltage Control of a van der Waals Spin-Filter Magnetic Tunnel Junction. *Nano Lett.* **19**, 915–920, DOI: 10.1021/acs.nanolett.8b04160 (2019).

109. Wang, Z. *et al.* Electric-field control of magnetism in a few-layered van der Waals ferromagnetic semiconductor. *Nat. Nanotechnol.* **13**, 554–559, DOI: 10.1038/s41565-018-0186-z (2018).

110. Sun, Y. *et al.* Effects of hydrostatic pressure on spin-lattice coupling in two-dimensional ferromagnetic $Cr_2Ge_2Te_6$. *Appl. Phys. Lett.* **112**, 72409, DOI: 10.1063/1.5016568 (2018).

111. Mondal, S. *et al.* Effect of hydrostatic pressure on ferromagnetism in two-dimensional CrI_3. *Phys. Rev. B* **99**, 180407, DOI: 10.1103/PhysRevB.99.180407 (2019). 1901.00706.

112. Lin, Z. *et al.* Pressure-induced spin reorientation transition in layered ferromagnetic insulator $Cr_2Ge_2Te_6$. *Phys. Rev. Mater.* **2**, 51004, DOI: 10.1103/PhysRevMaterials.2.051004 (2018).

113. Li, T. *et al.* Pressure-controlled interlayer magnetism in atomically thin CrI_3. *Nat. Mater.* **18**, 1303–1308, DOI: 10.1038/s41563-019-0506-1 (2019). 1905.10905.

114. Jiang, P. *et al.* Stacking tunable interlayer magnetism in bilayer CrI_3. *Phys. Rev. B* **99**, 144401, DOI: 10.1103/PhysRevB.99.144401 (2019). 1806.09274.

115. Jang, S. W., Jeong, M. Y., Yoon, H., Ryee, S. & Han, M. J. Microscopic understanding of magnetic interactions in bilayer CrI_3. *Phys. Rev. Mater.* **3**, 31001, DOI: 10.1103/PhysRevMaterials.3.031001 (2019). 1809.01388.

116. Sivadas, N., Okamoto, S., Xu, X., Fennie, C. J. & Xiao, D. Stacking-Dependent Magnetism in Bilayer CrI_3. *Nano Lett.* **18**, 7658–7664, DOI: 10.1021/acs.nanolett.8b03321 (2018). 1808.06559.

117. Soriano, D., Cardoso, C. & Fernández-Rossier, J. Interplay between interlayer exchange and stacking in CrI_3 bilayers. *Solid State Commun.* **299**, 113662, DOI: 10.1016/j.ssc.2019.113662 (2019). 1807.00357.

118. Klein, D. R. *et al.* Enhancement of interlayer exchange in an ultrathin two-dimensional magnet. *Nat. Phys.* **15**, 1255–1260, DOI: 10.1038/s41567-019-0651-0 (2019).

119. Kent, A. D. & Worledge, D. C. A new spin on magnetic memories. *Nat. Nanotechnol.* **10**, 187–191, DOI: 10.1038/nnano.2015.24 (2015).

120. Dieny, B. *et al.* Opportunities and challenges for spintronics in the microelectronics industry. *Nat. Electron.* **3**, 446–459, DOI: 10.1038/s41928-020-0461-5 (2020). 1908.10584.

121. Grollier, J. *et al.* Neuromorphic spintronics. *Nat. Electron.* **3**, 360–370, DOI: 10.1038/s41928-019-0360-9 (2020).

122. MacNeill, D. *et al.* Control of spin-orbit torques through crystal symmetry in WTe_2 /ferromagnet bilayers. *Nat. Phys.* **13**, 300–305, DOI: 10.1038/nphys3933 (2017). 1605.02712.

123. Guimarães, M. H., Stiehl, G. M., MacNeill, D., Reynolds, N. D. & Ralph, D. C. Spin-Orbit Torques in $NbSe_2$/Permalloy Bilayers. *Nano Lett.* **18**, 1311–1316, DOI: 10.1021/acs.nanolett.7b04993 (2018). 1801.07281.

124. Shi, S. *et al.* All-electric magnetization switching and Dzyaloshinskii–Moriya interaction in WTe_2/ferromagnet heterostructures. *Nat. Nanotechnol.* **14**, 945–949, DOI: 10.1038/s41565-019-0525-8 (2019).

125. Alghamdi, M. *et al.* Highly Efficient Spin-Orbit Torque and Switching of Layered Ferromagnet Fe_3GeTe_2. *Nano Lett.* **19**, 4400–4405, DOI: 10.1021/acs.nanolett.9b01043 (2019). 1903.00571.

126. Wang, X. *et al.* Current-driven magnetization switching in a van der Waals ferromagnet Fe_3GeTe_2. *Sci. Adv.* **5**, DOI: 10.1126/sciadv.aaw8904 (2019).

127. Ostwal, V., Shen, T. & Appenzeller, J. Efficient Spin-Orbit Torque Switching of the Semiconducting Van Der Waals Ferromagnet $Cr_2Ge_2Te_6$. *Adv. Mater.* **32**, 1–7, DOI: 10.1002/adma.201906021 (2020).

128. Ralph, D. & Stiles, M. Spin transfer torques. *J. Magn. Magn. Mater.* **320**, 1190–1216, DOI: 10.1016/j.jmmm.2007.12.019 (2008).

129. Avci, C. O. *et al.* Current-induced switching in a magnetic insulator. *Nat. Mater.* **16**, 309–314, DOI: 10.1038/nmat4812 (2017).

130. Shin, I. *et al.* Spin-orbit Torque Switching in an All-Van der Waals Heterostructure (2021). 2102.09300.

131. Fang, D. *et al.* Spin-orbit-driven ferromagnetic resonance. *Nat. Nanotechnol.* **6**, 413–417, DOI: 10.1038/nnano.2011.68 (2011).

132. Ciccarelli, C. *et al.* Room-temperature spin-orbit torque in NiMnSb. *Nat. Phys.* **12**, 855–860, DOI: 10.1038/nphys3772 (2016). 1510.03356.

133. Yoshimi, R. *et al.* Current-driven magnetization switching in ferromagnetic bulk Rashba semiconductor (Ge,Mn)Te. *Sci. Adv.* **4**, DOI: 10.1126/sciadv.aat9989 (2018).

134. Kurebayashi, H. *et al.* An antidamping spin-orbit torque originating from the Berry curvature. *Nat. Nanotechnol.* **9**, 211–217, DOI: 10.1038/nnano.2014.15 (2014).

135. Bradley, C. J. & Cracknell, A. P. *The Mathematical Theory of Symmetry in Solids: Representation theory for point groups and space groups* (Oxford University Press, 1972).

136. Manipatruni, S. *et al.* Scalable energy-efficient magnetoelectric spin–orbit logic. *Nature* **565**, 35–42, DOI: 10.1038/s41586-018-0770-2 (2019).

137. Bandyopadhyay, S. & Cahay, M. *Introduction to Spintronics* (CRC Press, 2008), first edn.

138. Kurz, P., Förster, F., Nordström, L., Bihlmayer, G. & Blügel, S. Ab initio treatment of noncollinear magnets with the full-potential linearized augmented plane wave method. *Phys. Rev. B* **69**, 024415, DOI: 10.1103/PhysRevB.69.024415 (2004).

139. Freimuth, F., Blügel, S. & Mokrousov, Y. Spin-orbit torques in Co/Pt(111) and Mn/W(001) magnetic bilayers from first principles. *Phys. Rev. B* **90**, 174423, DOI: 10.1103/PhysRevB.90.174423 (2014). 1305.4873.

140. Haney, P. M. *et al.* Current-induced order parameter dynamics: Microscopic theory applied to Co/Cu/Co. *Phys. Rev. B* **76**, 024404, DOI: 10.1103/PhysRevB.76.024404 (2007).

141. Garate, I. & MacDonald, A. H. Influence of a transport current on magnetic anisotropy in gyrotropic ferromagnets. *Phys. Rev. B* **80**, 134403, DOI: 10.1103/PhysRevB.80.134403 (2009). 0905.3856.

142. Dresselhaus, M. S., Dresselhaus, G. & Jorio, A. *Group theory*, vol. 53 (Springer Berlin Heidelberg, Berlin, Heidelberg, 2008).

143. Zollner, K. *et al.* Scattering-induced and highly tunable by gate damping-like spin-orbit torque in graphene doubly proximitized by two-dimensional magnet $Cr_2Ge_2Te_6$ and monolayer WS_2. *Phys. Rev. Res.* **2**, 1–12, DOI: 10.1103/physrevresearch.2.043057 (2020). 1910.08072.

144. Zihlmann, S. *et al.* Large spin relaxation anisotropy and valley-Zeeman spin-orbit coupling in WSe_2/Gr/hBN heterostructures. *Phys. Rev. B* **97**, 075434, DOI: 10.1103/PhysRevB.97.075434 (2018).

145. Manchon, A., Koo, H. C., Nitta, J., Frolov, S. M. & Duine, R. A. New perspectives for Rashba spin–orbit coupling. *Nat. Mater.* **14**, 871–882, DOI: 10.1038/nmat4360 (2015). 1507.02408.

146. Tuan, D. V., Ortmann, F., Soriano, D., Valenzuela, S. O. & Roche, S. Pseudospin-driven spin relaxation mechanism in graphene. *Nat. Phys.* **10**, 857–863, DOI: 10.1038/nphys3083 (2014).

147. Ok, S. *et al.* Custodial glide symmetry of quantum spin Hall edge modes in monolayer WTe_2. *Phys. Rev. B* **99**, 121105, DOI: 10.1103/PhysRevB.99.121105 (2019).

148. Garcia, J. H. *et al.* Canted Persistent Spin Texture and Quantum Spin Hall Effect in WTe_2. *Phys. Rev. Lett.* **125**, 256603, DOI: 10.1103/PhysRevLett.125.256603 (2020).

149. Liu, L. *et al.* Symmetry-dependent field-free switching of perpendicular magnetization. *Nat. Nanotechnol.* **16**, 277–282, DOI: 10.1038/s41565-020-00826-8 (2021).

150. Garello, K. *et al.* Symmetry and magnitude of spin-orbit torques in ferromagnetic heterostructures. *Nat. Nanotechnol.* **8**, 587–593, DOI: 10.1038/nnano.2013.145 (2013).

151. Belashchenko, K. D., Kovalev, A. A. & Van Schilfgaarde, M. First-principles calculation of spin-orbit torque in a Co/Pt bilayer. *Phys. Rev. Mater.* **3**, 11401, DOI: 10.1103/PhysRevMaterials.3.011401 (2019). 1810.11003.

152. Dolui, K. *et al.* Proximity Spin-Orbit Torque on a Two-Dimensional Magnet within van der Waals Heterostructure: Current-Driven Antiferromagnet-to-Ferromagnet Reversible Nonequilibrium Phase Transition in Bilayer CrI_3. *Nano Lett.* **20**, 2288–2295, DOI: 10.1021/acs.nanolett.9b04556 (2020).

153. Kochan, D., Irmer, S. & Fabian, J. Model spin-orbit coupling Hamiltonians for graphene systems. *Phys. Rev. B* **95**, 165415, DOI: 10.1103/PhysRevB.95.165415 (2017). 1610.08794.

154. Johansen, Ø., Risinggård, V., Sudbø, A., Linder, J. & Brataas, A. Current control of magnetism in two-dimensional fe_3gete_2. *Phys. Rev. Lett.* **122**, 217203, DOI: 10.1103/PhysRevLett.122.217203 (2019). 1812.06096.

155. Seemann, M., Ködderitzsch, D., Wimmer, S. & Ebert, H. Symmetry-imposed shape of linear response tensors. *Phys. Rev. B* **92**, 155138, DOI: 10.1103/PhysRevB.92.155138 (2015). 1507.04947.

156. MacNeill, D. *et al.* Thickness dependence of spin-orbit torques generated by WTe_2. *Phys. Rev. B* **96**, 054450, DOI: 10.1103/PhysRevB.96.054450 (2017). 1707.03757.

157. Gupta, V. *et al.* Manipulation of the van der Waals Magnet $Cr_2Ge_2Te_6$ by Spin-Orbit Torques. *Nano Lett.* **20**, 7482–7488, DOI: 10.1021/acs.nanolett.0c02965 (2020).

158. Cheng, C., Sun, J. T., Chen, X. R., Fu, H. X. & Meng, S. Nonlinear Rashba spin splitting in transition metal dichalcogenide monolayers. *Nanoscale* **8**, 17854–17860, DOI: 10.1039/c6nr04235j (2016).

159. Shao, Q. *et al.* Strong Rashba-Edelstein Effect-Induced Spin–Orbit Torques in Monolayer Transition Metal Dichalcogenide/Ferromagnet Bilayers. *Nano Lett.* **16**, 7514–7520, DOI: 10.1021/acs.nanolett.6b03300 (2016).

160. Zhang, W. *et al.* Research Update: Spin transfer torques in permalloy on monolayer MoS_2. *APL Mater.* **4**, 32302, DOI: 10.1063/1.4943076 (2016).

161. Husain, S. *et al.* Emergence of spin–orbit torques in 2D transition metal dichalcogenides: A status update. *Appl. Phys. Rev.* **7**, 041312, DOI: 10.1063/5.0025318 (2020).

162. Hidding, J. & Guimarães, M. H. Spin-Orbit Torques in Transition Metal Dichalcogenide/Ferromagnet Heterostructures. *Front. Mater.* **7**, DOI: 10.3389/fmats.2020.594771 (2020).

163. Lv, W. *et al.* Electric-Field Control of Spin-Orbit Torques in WS_2/Permalloy Bilayers. *ACS Appl. Mater. Interfaces* **10**, 2843–2849, DOI: 10.1021/acsami.7b16919 (2018).

164. Stiehl, G. M. *et al.* Layer-dependent spin-orbit torques generated by the centrosymmetric transition metal dichalcogenide β-$MoTe_2$. *Phys. Rev. B* **100**, DOI: 10.1103/PhysRevB.100.184402 (2019). 1906.01068.

165. Xie, Q. *et al.* Giant Enhancements of Perpendicular Magnetic Anisotropy and Spin-Orbit Torque by a MoS_2 Layer. *Adv. Mater.* **31**, 1–9, DOI: 10.1002/adma.201900776 (2019).

166. Liang, S. *et al.* Spin-Orbit Torque Magnetization Switching in $MoTe_2$/Permalloy Heterostructures. *Adv. Mater.* **32**, 1–6, DOI: 10.1002/adma.202002799 (2020).

167. Haastrup, S. *et al.* The Computational 2D Materials Database: High-throughput modeling and discovery of atomically thin crystals. *2D Mater.* **5**, 042002, DOI: 10.1088/2053-1583/aacfc1 (2018). 1806.03173.

168. Lu, A. Y. *et al.* Janus monolayers of transition metal dichalcogenides. *Nat. Nanotechnol.* **12**, 744–749, DOI: 10.1038/nnano.2017.100 (2017).

169. Zhang, J. *et al.* Janus Monolayer Transition-Metal Dichalcogenides. *ACS Nano* **11**, 8192–8198, DOI: 10.1021/acsnano.7b03186 (2017). 1704.06389.

170. Gambardella, P. & Miron, I. M. Current-induced spin–orbit torques. *Philos. Transactions Royal Soc. A: Math. Phys. Eng. Sci.* **369**, 3175–3197, DOI: 10.1098/rsta.2010.0336 (2011).

171. Hayashi, M., Kim, J., Yamanouchi, M. & Ohno, H. Quantitative characterization of the spin-orbit torque using harmonic Hall voltage measurements. *Phys. Rev. B* **89**, 144425, DOI: 10.1103/PhysRevB.89.144425 (2014).

172. Liu, L., Moriyama, T., Ralph, D. C. & Buhrman, R. A. Spin-torque ferromagnetic resonance induced by the spin Hall effect. *Phys. Rev. Lett.* **106**, 36601, DOI: 10.1103/PhysRevLett.106.036601 (2011). 1011.2788.

173. Mecking, N., Gui, Y. S. & Hu, C.-M. Microwave photovoltage and photoresistance effects in ferromagnetic microstrips. *Phys. Rev. B* **76**, 224430, DOI: 10.1103/PhysRevB.76.224430 (2007).

174. Fan, Z. *et al.* Linear scaling quantum transport methodologies. *Phys. Reports* **903**, 1–69, DOI: 10.1016/j.physrep.2020.12.001 (2021). 1811.07387.

175. Lee, K.-S. *et al.* Angular dependence of spin-orbit spin-transfer torques. *Phys. Rev. B* **91**, 144401, DOI: 10.1103/PhysRevB.91.144401 (2015). 1409.5600.

176. Sousa, F., Tatara, G. & Ferreira, A. Skew-scattering-induced giant antidamping spin-orbit torques: Collinear and out-of-plane Edelstein effects at two-dimensional material/ferromagnet interfaces. *Phys. Rev. Res.* **2**, 43401, DOI: 10.1103/physrevresearch.2.043401 (2020).

177. Xue, F., Rohmann, C., Li, J., Amin, V. & Haney, P. Unconventional spin-orbit torque in transition metal dichalcogenide-ferromagnet bilayers from first-principles calculations. *Phys. Rev. B* **102**, 14401, DOI: 10.1103/PhysRevB.102.014401 (2020). 2005.01109.

178. Mahfouzi, F., Mishra, R., Chang, P. H., Yang, H. & Kioussis, N. Microscopic origin of spin-orbit torque in ferromagnetic heterostructures: A first-principles approach. *Phys. Rev. B* **101**, 60405, DOI: 10.1103/PhysRevB.101.060405 (2020).

179. Nikolić, B. K. *et al.* First-principles quantum transport modeling of spin-transfer and spin-orbit torques in magnetic multilayers. In *arXiv*, 1–35, DOI: 10.1007/978-3-319-50257-1_112-1 (Springer International Publishing, Cham, 2018). 1801.05793.

180. Fan, X. *et al.* Quantifying interface and bulk contributions to spin–orbit torque in magnetic bilayers. *Nat. Commun.* **5**, 3042, DOI: 10.1038/ncomms4042 (2014).

181. Taniguchi, T., Grollier, J. & Stiles, M. D. Spin-transfer torques generated by the anomalous hall effect and anisotropic magnetoresistance. *Phys. Rev. Appl.* **3**, 044001, DOI: 10.1103/PhysRevApplied.3.044001 (2015).

182. Baek, S.-h. C. *et al.* Spin currents and spin–orbit torques in ferromagnetic trilayers. *Nat. Mater.* **17**, 509–513, DOI: 10.1038/s41563-018-0041-5 (2018).

183. Iihama, S. *et al.* Spin-transfer torque induced by the spin anomalous hall effect. *Nat. Electron.* **1**, 120–123, DOI: 10.1038/s41928-018-0026-z (2018).

184. Sierra, J. F., Fabian, J., Kawakami, R. K., Roche, S. & Valenzuela, S. O. Van der waals heterostructures for spintronics and opto-spintronics. *Nat. Nanotechnol.* DOI: 10.1038/s41565-021-00936-x (2021).

185. Bhatti, S. *et al.* Spintronics based random access memory: a review. *Mater. Today* **20**, 530–548, DOI: 10.1016/j.mattod.2017.07.007 (2017).

186. Zheng, S. *et al.* High-Temperature Ferromagnetism in an Fe_3P Monolayer with a Large Magnetic Anisotropy. *J. Phys. Chem. Lett.* **10**, 2733–2738, DOI: 10.1021/acs.jpclett.9b00970 (2019).

187. Torelli, D., Thygesen, K. S. & Olsen, T. High throughput computational screening for 2d ferromagnetic materials: the critical role of anisotropy and local correlations. *2D Mater.* **6**, 045018, DOI: 10.1088/2053-1583/ab2c43 (2019).

188. Wadley, P. *et al.* Electrical switching of an antiferromagnet. *Science* DOI: 10.1126/science.aab1031 (2016). https://science.sciencemag.org/content/early/2016/01/13/science.aab1031.full.pdf.

189. Jungwirth, T. *et al.* The multiple directions of antiferromagnetic spintronics. *Nat. Phys.* **14**, 200–203, DOI: 10.1038/s41567-018-0063-6 (2018).

190. Seixas, L., Rodin, A. S., Carvalho, A. & Castro Neto, A. H. Multiferroic Two-Dimensional Materials. *Phys. Rev. Lett.* **116**, 206803, DOI: 10.1103/PhysRevLett.116.206803 (2016). 1601.06438.

191. Huang, C. *et al.* Prediction of Intrinsic Ferromagnetic Ferroelectricity in a Transition-Metal Halide Monolayer. *Phys. Rev. Lett.* **120**, 147601, DOI: 10.1103/PhysRevLett.120.147601 (2018).

192. Yang, Q., Xiong, W., Zhu, L., Gao, G. & Wu, M. Chemically Functionalized Phosphorene: Two-Dimensional Multiferroics with Vertical Polarization and Mobile Magnetism. *J. Am. Chem. Soc.* **139**, 11506–11512, DOI: 10.1021/jacs.7b04422 (2017).

193. Xu, M. *et al.* Electrical Control of Magnetic Phase Transition in a Type-I Multiferroic Double-Metal Trihalide Monolayer. *Phys. Rev. Lett.* **124**, 67602, DOI: 10.1103/PhysRevLett.124.067602 (2020).

194. Li, J. *et al.* Intrinsic magnetic topological insulators in van der Waals layered $MnBi_2Te_4$ -family materials. *Sci. Adv.* **5**, eaaw5685, DOI: 10.1126/sciadv.aaw5685 (2019).

195. Wu, J. *et al.* Natural van der Waals heterostructural single crystals with both magnetic and topological properties. *Sci. Adv.* **5**, DOI: 10.1126/sciadv.aax9989 (2019).

196. Hu, C. *et al.* A van der Waals antiferromagnetic topological insulator with weak interlayer magnetic coupling. *Nat. Commun.* **11**, 97, DOI: 10.1038/s41467-019-13814-x (2020).

197. Deng, Y. *et al.* Quantum anomalous Hall effect in intrinsic magnetic topological insulator $MnBi_2Te_4$. *Science* **367**, 895–900, DOI: 10.1126/science.aax8156 (2020). 1904.11468.

198. Mellnik, A. R. *et al.* Spin-transfer torque generated by a topological insulator. *Nature* **511**, 449–451, DOI: 10.1038/nature13534 (2014).

199. Yang, M. *et al.* Creation of skyrmions in van der Waals ferromagnet Fe_3GeTe_2 on (Co/Pd)n superlattice. *Sci. Adv.* **6**, DOI: 10.1126/sciadv.abb5157 (2020).

200. Wu, Y. *et al.* Néel-type skyrmion in WTe_2/Fe_3GeTe_2 van der Waals heterostructure. *Nat. Commun.* **11**, 3860, DOI: 10.1038/s41467-020-17566-x (2020). 1907.11349.

201. Park, T.-E. *et al.* Néel-type skyrmions and their current-induced motion in van der Waals ferromagnet-based heterostructures. *Phys. Rev. B* **103**, 104410, DOI: 10.1103/PhysRevB.103.104410 (2021). 1907.01425.

202. Zhang, X.-X. *et al.* Gate-tunable spin waves in antiferromagnetic atomic bilayers. *Nat. Mater.* **19**, 838–842, DOI: 10.1038/s41563-020-0713-9 (2020).

203. McCreary, A. *et al.* Distinct magneto-Raman signatures of spin-flip phase transitions in CrI_3. *Nat. Commun.* **11**, 3879, DOI: 10.1038/s41467-020-17320-3 (2020). 1910.01237.

204. Cenker, J. *et al.* Direct observation of two-dimensional magnons in atomically thin CrI_3. *Nat. Phys.* **17**, 20–25, DOI: 10.1038/s41567-020-0999-1 (2021).

205. Huang, B. *et al.* Emergent phenomena and proximity effects in two-dimensional magnets and heterostructures. *Nat. Mater.* **19**, 1276–1289, DOI: 10.1038/s41563-020-0791-8 (2020).

206. Giustino, F. *et al.* The 2021 quantum materials roadmap. *J. Physics: Mater.* **3**, 042006, DOI: 10.1088/2515-7639/abb74e (2021).

Acknowledgements

H. K. and S. K. acknowledge supports from EPSRC via EP/T006749/1 and also help by Oscar Lee for producing graphical images. S. R. and J. H. G. acknowledge funding from the European Union Seventh Framework Programme under Grant No. 881603 (Graphene Flagship) and the King Abdullah University of Science and Technology (KAUST) through award number OSR-2018-CRG7-3717. ICN2 is funded by the CERCA Programme/Generalitat de Catalunya and supported by the Severo Ochoa programme (MINECO Grant. No. SEV-2017-0706).

Author contributions

The authors contributed to all aspects of the article.

Competing interests

The authors declare no competing interests.

Peer Review Information

Nature Reviews Physics thanks Kyung-Jin Lee and other anonymous reviewers for their contribution to the peer review of this work.

Figure 6. Experimentally validated critical magnetic transition temperature, (T_C) for various 2D van der Waals (vdWs) magnetic systems. a | 2D vdW magnetic materials library showing experimentally determined magnetic transition temperature for materials in insulating and metallic phases. In the insulating phase, number in brackets corresponds to the bandgap value. The dataset is characterised in two-ways using the colours and symbols. Colours: red (ferromagnetic ordering), blue (anti-ferromagnetic ordering). Symbols: bar (top and bottom points in the bar highlight the transition temperature for bulk and mono/few-layers, respectively), △ (T_C is reported for the bulk case), ◯ (T_C is identified for mono/few-layers), ◊ (T_C is independent of material thickness), and ★ (T_C is enhanced by the external techniques). **b** | Three different exchange coupling mechanisms of two individual moments as an underlying origin of the long-range magnetic ordering for material systems in the insulating and metallic phases going from left to right. Data in panel a are taken from Refs.[1,14,26,29–31,55–57,61–93].

Figure 7. Experimental observation of electric field control of magnetism in different van der Waals (vdW) magnets. a | A schematic side view of a field-effect device with a bilayer CrI_3 encapsulated in few-layer graphene and hBN. The right panel is an optical microscope image for the device. **b** | Electric field control of magnetism. The critical temperature, T_C, is measured as ac susceptibility with different gate voltages. **c** | Coercive force, H_c, (magenta), saturation magnetization, M_S, (purple) (both at 4 K) and T_C (orange) normalized by their values at zero gate voltage as a function of gate voltage, V_G, and induced doping density. **d** | Schematic of a field-effect-transistor device with $Cr_2Ge_2Te_6$ and side view of charge accumulation, n, by electric field. V_{DS}, source-drain bias. **e** | Experimentally-deduced out-of-plane anisotropy field, H_u, in $Cr_2Ge_2Te_6$ as a function of temperature, T, for different gate voltages. **f** | Hysteresis loops of trilayer Fe_3GeTe_2 at different temperatures. R_{xy}, transverse resistance; $\mu_0 H_C$, applied field. **g** | T_C dependence on V_G in trilayer Fe_3GeTe_2. **h** | T_C of Fe_3GeTe_2 with different layer thicknesses measured by different analysis methods shown. **i** | Extracted critical field, $\mu_0 H_C$, for spin-flip transition and T_C as a function of pressure in a trilayer CrI_3. Panel a-c adapted from Ref.[102], panels d and e adapted from Ref.[61], panelf f-h adapted from Ref.[30] and panel i adapted from Ref.[103].

Figure 8. Illustration of spin-orbit torque mechanisms for different spin-textures and their effects on the magnetic energy profile. a | Magnetization dynamics due to a typical effective spin-orbit torque field for systems with multiple orthogonal mirror planes. **b** | Magnetization dynamics for effective spin-orbit coupling (SOC) fields with a component parallel to the anisotropy axis. **c** | Magnetic energy density for a system with perpendicular magnetic anisotropy and a weak in-plane effective SOC field produced an in-plane spin texture. **d** | Magnetic energy density for a system with perpendicular magnetic anisotropy and an effective field with a component parallel to the anisotropy axis, and the spin-textures that enable these kind of fields. **m**, magnetization; **H**, magnetic field strength; **J**, current

.

Figure 9. Distributions of magnetic materials predicted using first principle calculations as a function of their symmetry The materials family, which requires a substrate-induced inversion symmetry breaking to generate torque components, is identified by the filled blue histograms. Non-centrosymmetric materials which may manifest SOT are outlined by filled red histograms.

Box1

The C_{3v} point group of symmetries possess a generating set given by a 120° rotation around the z-axis and a reflection on the yz plane. For any possible symmetries $\mathcal{R}$, the matrices Y and Λ must satisfy the following set of equations[139,155] $\mathrm{Y} = \det(\mathcal{R})\,\mathcal{R}\mathrm{Y}\mathcal{R}^T$ and $\Lambda^i = \sum_{i'=x,y,z} \mathcal{R}_{i,i'}\mathcal{R}\Lambda^{i'}\mathcal{R}^T$, where $i,j,k \in (x,y,z)$ defining the direction of the axes of a chosen Cartesian system. Here we show how these tensors change after successive application of the two symmetries. The matrix Y is antisymmetric and translate into a cross product between the current and the rotation axis $\mathbf{H}^e = \mathrm{Y}_{yx}\mathbf{J} \times \hat{\boldsymbol{z}}$. The second term is less straightforward but it is, still, fully defined by just five parameters, that reduces to three for 2D materials. This is a substantial reduction in the number of degree of freedom that one would, for example, use in a phenomenological fit of the experiment. Also, note that a microscopic calculation would automatically give such reduction, which can be used as a check, or simply one can use the symmetry to reduce calculation cost.

Website summary

Spintronic properties of layered materials combining magnetism and strong spin-orbit coupling can be tailored by proper optimization of chemical interactions and structural material symmetries. This Review draws a route to achieving best performing material design for reaching the upper limit of spin-orbit torque efficiency in switching magnetization.